OPEN ACCESS



DIISC-III. Signatures of Stellar Disk Growth in Nearby Galaxies

Mansi Padave ¹, Sanchayeeta Borthakur ¹, Hansung B. Gim ², David Thilker ³, Rolf A. Jansen ¹, Jacqueline Monkiewicz ¹, Robert C. Kennicutt ^{4,5}, Guinevere Kauffmann Andrew J. Fox ⁷, Emmanuel Momjian ⁸, and Timothy Heckman ³, School of Earth & Space Exploration, Arizona State University, Tempe, AZ 85287-1404, USA ² Department of Physics, Montana State University, P.O. Box 173840, Bozeman, MT 59717, USA ³ Department of Physics & Astronomy, Johns Hopkins University, Baltimore, MD 21218, USA ⁴ Department of Astronomy and Steward Observatory, University of Arizona, Tucson, AZ 85721, USA ⁵ Department of Physics and Astronomy, Texas A&M University, College Station, TX 77843, USA ⁶ Max-Planck-Institute für Astrophysik, Karl-Schwarzschild-Straße 1, D-85740 Garching, Germany AURA for ESA, Space Telescope Science Institute, 3700 San Martin Drive, Baltimore, MD 21218, USA National Radio Astronomy Observatory, 1003 Lopezville Road, Socorro, NM 87801, USA Received 2023 August 14; revised 2023 September 29; accepted 2023 October 10; published 2023 December 19

Abstract

We explore the growth of the stellar disks in 14 nearby spiral galaxies as part of the Deciphering the Interplay between the Interstellar medium, Stars, and the Circumgalactic medium (DIISC) survey. We study the radial distribution of specific star formation rates (sSFRs) and investigate the ratio of the difference in the outer and inner sSFRs ($\Delta_{\rm sSFR} = {\rm sSFR_{out}} - {\rm sSFR_{in}}$) of the disk and the total sSFR, $\Delta_{\rm sSFR}/{\rm sSFR}$, to quantify disk growth. We find $\Delta_{\rm sSFR}/{\rm sSFR}$ and the H I gas fraction to show a mild correlation of Spearman's $\rho=0.30$, indicating that star formation and disk growth are likely to proceed outward in galactic disks with high H I gas fractions. The H I gas fractions and $\Delta_{\rm sSFR}/{\rm sSFR}$ of the galaxies also increase with the distance to the nearest L_{\star} neighbor, suggesting that galaxies are likely to sustain the cold gas in their interstellar medium and exhibit inside-out growth in isolated environments. However, the H I content in their circumgalactic medium (CGM), probed by the Ly α equivalent width ($W_{\rm Ly}\alpha$) excess, is observed to be suppressed in isolated environments, as is apparent from the strong anticorrelation between the $W_{\rm Ly}\alpha$ excess and the distance to the fifth nearest L_{\star} neighbor (Spearman's $\rho=-0.62$). As expected, $W_{\rm Ly}\alpha$ is also found to be suppressed in cluster galaxies. We find no relation between the $W_{\rm Ly}\alpha$ excess of the detected CGM absorber and $\Delta_{\rm sSFR}/{\rm sSFR}$, implying that the enhancement and suppression of the circumgalactic H I gas does not affect the direction in which star formation proceeds in a galactic disk or vice versa.

Unified Astronomy Thesaurus concepts: Spiral galaxies (1560); Disk galaxies (391); Star formation (1569); Interstellar medium (847); H I line emission (690); Circumgalactic medium (1879)

Supporting material: figure sets

1. Introduction

The growth of galactic stellar disks is a well-studied quantitative tracer of galaxy evolution. Disk growth requires the accretion of gas (Birnboim & Dekel 2003; Kereš et al. 2005) onto the galactic disk, much of which is eventually turned into stars. According to the classical paradigm, cold low-metallicity gas from the intergalactic medium travels through the circumgalactic medium (CGM) of the galaxy and condenses onto the H I disk (Sancisi et al. 2008, and references therein). There, it nurtures and sustains star formation, leading to stellar build-up and disk growth.

If the gas accretion at later times occurs predominantly at large radii, the galactic disk is then said to grow *inside-out*, i.e., the outer stellar disk forms at a later stage than the inner disk, causing an increase in scale lengths (Larson 1976; Fall & Efstathiou 1980; White & Frenk 1991; Mo et al. 1998; Naab & Ostriker 2006; Somerville et al. 2008; Dutton et al. 2011). Simulations indeed show that gas with higher angular momentum is being accreted onto the outer disk at later times and increasing the star formation timescale with galactocentric radius (Sommer-Larsen & Dolgov 2001; Samland &

Original content from this work may be used under the terms of the Creative Commons Attribution 4.0 licence. Any further distribution of this work must maintain attribution to the author(s) and the title of the work, journal citation and DOI.

Gerhard 2003; Brook et al. 2006, 2012; Roškar et al. 2008, 2010; Pilkington et al. 2012; Avila-Reese et al. 2018).

On the observational front, the stellar mass-size relation shows that for the same stellar mass bin, galaxies at high redshift $(z \gtrsim 2)$ were smaller (Ferguson et al. 2004; Barden et al. 2005; Buitrago et al. 2008; Franx et al. 2008; van Dokkum et al. 2013; Rodríguez-Puebla et al. 2017). In the local Universe ($z \le 0.5$), observations of radial color and metallicity gradients show that young stars are spatially extended compared to the more centrally concentrated old stellar populations (MacArthur et al. 2004; Muñoz-Mateos et al. 2007, 2011; Wang et al. 2011; Pezzulli et al. 2015; Lian et al. 2017). Studies of the star formation history of the Milky Way (Frankel et al. 2019), and the Local Group (NGC 300, M33, NGC 7793; Gogarten et al. 2009; Williams et al. 2009; Sacchi et al. 2019) also advocate for the inside-out mode of disk growth. Multiple studies of resolved stellar photometry that modeled the star formation history stipulate that younger stellar populations extend farther out into the galactic disk (Bell & de Jong 2000; Brown et al. 2008; González Delgado et al. 2014; Dale et al. 2016, 2020; Goddard et al. 2017; Smith et al. 2022).

The presence of an extended ultraviolet (XUV) disk in nearby galaxies (Thilker et al. 2007; Lemonias et al. 2011), indicative of relatively recent star formation beyond the optical disk ($\gtrsim R_{25}$), provides evidence of the inside-out mode of growth. In Padave et al. (2021), we inspected the XUV disk galaxy, NGC 3344, and observed a radial increase in the

specific star formation rates from $10^{-10}~\rm yr^{-1}$ to $10^{-8}~\rm yr^{-1}$, hinting toward an outward growing disk. We also detected a strong absorption component with a velocity offset of $113~\rm km~s^{-1}$ in the CGM, which was interpreted as inflowing gas that may gradually accrete onto the galaxy's H I disk and serve as the fuel for star formation. The approach of probing the CGM alongside the interstellar medium (ISM) and star formation is crucial to understanding disk growth.

In this study, we investigate the radial distribution of star formation, stellar mass, and H I gas in 14 nearby galaxies from the Deciphering the Interplay between the Interstellar medium, Stars, and the Circumgalactic medium survey (DIISC; S. Borthakur et al. 2024, in preparation). The objective is to connect the growth of the stellar disk to the ISM, CGM, and local environment utilizing panchromatic data. We have ultraviolet (UV) absorption spectroscopy from the Cosmic Origins Spectrograph (COS; Green et al. 2012) aboard the Hubble Space Telescope (HST) combined with archival far-UV (FUV) and near-UV (NUV) imaging from Galaxy Evolution Explorer (GALEX), and we obtained deep optical g, r, and $H\alpha$ imaging with the Vatican Advanced Technology Telescope (VATT), and H I 21 cm imaging using the NSF's Karl G. Jansky Very Large Array (VLA). Together, these data provide information on the absorbers in the CGM, star formation rates, stellar masses, and cold HI gas in the ISM for the 14 low-z galaxies, enabling us to analyze the nature of stellar disk growth in the context of the cosmic baryon cycle.

The paper is organized as follows. A detailed description of the sample and the data used in this study is presented in Section 2, and the adopted methods to derive the star formation rates, stellar mass, and gas mass are discussed in Section 3. In Section 4, we present the surface brightness profiles and radial profiles of the surface density of stellar mass $(\Sigma_{M_{\star}})$, H I mass (Σ_{HI}) , and SFR (Σ_{SFR}) . We discuss the connection of stellar disk growth with atomic gas and galaxy environment in Section 5. Lastly, we summarize our results in Section 6.

2. Sample and Data

Our sample consists of 14 spiral galaxies selected from the DIISC survey (S. Borthakur et al. 2024, in preparation) based on the following criteria: (1) the galaxies lie within 120 Mpc of the Milky Way, (2) they have a background UV-bright quasistellar object (QSO) within 3.5 times the size of the H I disk, and (3) they were observed by GALEX (see Section 2.1.1). The size of the H I disk is defined as the radius deprojected at $\Sigma_{\rm HI} = 1\,M_{\odot}\,{\rm pc}^{-2}$. Table 1 lists the galaxies, their redshifts, our adopted distances in Mpc, and scale in pc/arcsec along with other properties (see Sections 2.5 and 3 for details). References for distances are listed in the notes to the table. For galaxies where direct measurements of distances were not available, we estimated the distances using the Cosmicflows-3 distance-velocity calculator (Kourkchi et al. 2020).

2.1. Observations

2.1.1. Ultraviolet Imaging Data

Archival FUV and NUV images from GALEX (Martin et al. 2005; Morrissey et al. 2007) were obtained from the Mikulski

Archive for Space Telescopes. GALEX carried out the All-Sky Imaging Survey with typical exposures of $\sim\!100\,\mathrm{s}$, the Medium Imaging Survey (MIS) and Nearby Galaxy Survey (NGS), and the Guest Investigator (GII) program with typical exposures of $\sim\!1500\,\mathrm{s}$ each (Bianchi et al. 2003; Morrissey et al. 2007). The selection of the galaxies was based on both the availability of deep UV imaging and their UV flux. The galaxies have either apparent FUV magnitudes $\leq\!16$ or deep MIS/NGS/GII observations to be able to investigate the flux distribution within their disk. IC 3440 and NGC 4921 have deep NGS and GII imaging but FUV magnitudes of 17.5 and 17.0, respectively. All galaxies, except NGC 3810, have MIS/NGS/GII observations in at least one of the bands.

The FUV and NUV stacks for each galaxy were produced by coadding all available individual data sets mentioned above. Final count maps were created by multiplying the intensity (counts/s) map with each galaxy's high-resolution relative response (s) map. The sky background was estimated from source-free regions and removed from each stack. The resulting FUV maps are shown in Figure 1. FUV and NUV flux densities were also corrected for foreground reddening using the E (B-V) values from Schlafly & Finkbeiner (2011) and $A_{\rm FUV}=7.9\times E(B-V)$ and $A_{\rm NUV}=8.0\times E(B-V)$ derived by Cardelli et al. (1989). The 1σ noise equivalent surface brightnesses for the FUV and NUV maps are 27.20 mag arcsec $^{-2}$ and 26.84 mag arcsec $^{-2}$, respectively. The FUV ($\lambda_{\rm eff}\sim 1538.6$ Å) and NUV ($\lambda_{\rm eff}\sim 2315.7$ Å) maps have angular resolutions (FWHM) of $4\rlap.{''}2$ and $5\rlap.{''}3$, respectively, and a pixel scale of $1\rlap.{''}5$.

2.2. Optical Imaging Data

We imaged each of our sample galaxies in Sloan g and r filters (henceforth, g and r) with the VATT4k CCD imager on the 1.8 m Vatican Advanced Technology Telescope (VATT) at the Mt. Graham Observatory. These observations were carried out along with other observations for the DIISC survey under the H α -DIISC program (M. Padave et al. in preparation) and were conducted over a period of 19 nights from 2019 March to 2021 March. The seeing FWHM on these nights was between 0."8 and 1."8.

Each galaxy was observed with a total integration time of 600 s in g and 1200 s in r. Bias-subtracted and flat-fielded (using both dome and twilight sky flats) science images were created using standard image processing routines in the Image Reduction and Analysis Facility. The sky background level was estimated from the average intensity in the sourcefree regions of each science image and subtracted. The cosmic-ray-induced signal was removed using the L.A. COSMIC routine (van Dokkum 2001). To create the final images in g and r for each galaxy, the science exposures were aligned using field stars, smoothed to match the resolution of the image with the worst seeing, and weighted by exposure time before combining. Flux calibration was performed using the Aperture Photometry Tool (Laher et al. 2012) and field stars. Instrumental magnitudes of the field stars were determined through aperture photometry from the g and rimages and matched to the Sloan Digital Sky survey (SDSS) DR7 catalog to derive the photometric zero-point of the images. The photometric zero-point of the g and r images was then calculated by comparing the instrumental magnitudes to their corresponding SDSS magnitudes for the same stars. The resulting r maps of our galaxies are shown in

⁹ The National Radio Astronomy Observatory is a facility of the National Science Foundation operated under a cooperative agreement by Associated Universities, Inc.

Table 1
Information on the Sample

Galaxy	z	Distance	Scale	$\log_{10}(M_{\star}/M_{\odot})$	$\log_{10}(SFR/M_{\odot} \text{ yr}^{-1})$	$\log_{10}(M_{\rm HI}/M_{\odot})$	ρ	$\log_{10}(W/\overline{W})_{{ m Ly}lpha}$
(1)	(2)	(Mpc) (3)	(pc/arcsec) (4)	(5)	(6)	(7)	(kpc) (8)	(9)
NGC 99	0.01772	79.4ª	378.17	10.62	0.39	10.35	163	0.107
NGC 3344	0.00196	8.28 ^b	40.14	10.18	-0.33	9.44	31	-0.248
NGC 3351	0.00259	9.29 ^b	45.04	10.90	-0.10	9.00	29	0.320
NGC 3433	0.00908	44.59	216.17	10.85	0.08	10.16	128	-0.207
NGC 3485	0.00477	29.43	142.68	10.45	-0.08	9.75	83	-0.134
NGC 3666	0.00353	17.1°	82.90	10.31	-0.49	9.44	56	-0.086
NGC 3810	0.00331	15.3°	74.18	10.44	0.10	9.43	41	0.053
NGC 4303	0.00522	18.7 ^d	90.66	11.39	0.72	9.88	26	0.561
NGC 4321	0.00525	13.93 ^e	67.53	10.58	0.40	9.38	39	-0.787
IC 3440	0.02597	120.46	584.01	10.22	-0.31	9.73	83	0.140
NGC 4921	0.01822	88.30 ^f	360.12	11.80	-0.25	9.20	53	-1.206
UGC 9120	0.01918	77.26	374.56	11.11	0.13	9.65	90	-0.140
NGC 5669	0.00456	14.5 ^g	70.30	9.52	-0.54	9.23	26	
NGC 5951	0.00593	27.1 ^g	131.38	10.10	-0.65	9.53	55	-0.037

Notes. Column (1): galaxies in our sample. Columns (2) and (3): redshift and adopted distances in Mpc. Column (4): scale in pc/arcsec. Columns (5), (6), and (7): stellar mass, star formation rate, and H I mass for our galaxies described in Section 3. $M_{\rm HI}$ estimates are adopted from ALFALFA (Haynes et al. 2018). Columns (8) and (9): impact parameters of the QSO sightline and the Ly α equivalent width excess described in Section 2.5.

Figure 2. The 1σ noise equivalent mean surface brightnesses of the final g and r maps are $25.57 \,\mathrm{mag\,arcsec^{-2}}$ and $25.44 \,\mathrm{mag\,arcsec^{-2}}$, respectively.

2.3. Infrared Imaging Data

Archival 24 μ m images taken with the Multiband Imaging Photometer for Spitzer (MIPS; Rieke et al. 2004) are available for six galaxies in our sample (NGC 3344, NGC 3351, NGC 3666, NGC 4303, NGC 4321, and NGC 5669). These maps have a resolution of 6". We also utilize archival 22 μ m imaging from the Wide-field Infrared Survey Explorer (WISE) All-Sky Data Release (Wright et al. 2010) for the remaining galaxies. These maps have a resolution of 11."8. All galaxies, except IC 3440, show emission in the 22 μ m maps.

2.4. VLA H I Data

The H I observations were conducted using the VLA under the VLA-DIISC program (P.I. S. Borthakur; H. B. Gim et al. 2023, in preparation) and project codes 17A-090, 18A-006, 19B-183, and 20A-125. Most galaxies were observed in the VLA D-configuration (maximum baseline, $b_{\rm max}=1$ km) with follow-up for some in B- and C-configurations ($b_{\rm max}=1.1$ km and $b_{\rm max}=3.4$ km, respectively). No VLA observations are available for IC 3440. Data were reduced using the Common Astronomy Software Application (CASA, CASA Team et al. 2022). A semiautomatic pipeline was used to solve for the delay, bandpass, amplitude, and phase gain calibrations. Hanning smoothing was implemented to mitigate the presence of Gibbs ringing artifacts, resulting in a reduction of the spectral (velocity) resolution to twice the original channel width. Specifically, the velocity resolution for the image cubes

of NGC 99 and NGC 9120 was set at 2.2 km s⁻¹, while the remaining image cubes maintained a velocity resolution of 3.3 km s⁻¹, with the exception of NGC 4921. In the case of NGC 4921, the image cube was generated using a velocity resolution of 20 km s⁻¹, strategically applied to enhance the signal-to-noise ratio through supplementary spectral axis smoothing. Data affected by radio-frequency interference were also edited out. The observation details, including project code, total integration time, flux density/bandpass and phase calibrators, synthesized beam sizes, velocity resolutions, and sensitivities of the resulting image cubes, are summarized in Table 2.

The spectral line visibilities were obtained using the CASA task *uvcontsub* by subtracting the continuum and used to produce H I image cubes with the CASA task *tclean*. We applied the Clark point-spread function and BARY spectral frame in general. We made the H I image cubes using the Briggs weighting function with a robust value of 0.5 for optimal sensitivity and synthesized beam size, except for NGC 4321. For NGC 4321, a uniform weighting function was used instead. More details about NGC 4321 and NGC 3344 can be found in Gim et al. (2021) and Padave et al. (2021), respectively.

2.5. COS Absorption Line Spectra

To probe the disk–CGM interface of the sample, UV absorption line spectroscopic observations of background UV-bright quasars were carried out with the G130M grating of COS (Green et al. 2012) aboard HST. These observations were conducted as part of the COS–DIISC Survey (HST Program ID: 14071; S. Borthakur et al. 2024, in preparation). The spectral resolution of the data was $\approx 20 \,\mathrm{km \, s^{-1}}$ ($R \sim 15,000$), covering a

^a Sánchez et al. (2012).

^b Sabbi et al. (2018).

^c Tully et al. (2016).

^d Pejcha & Prieto (2015).

e Hoeflich et al. (2017).

Lee & Jang (2016).

^g Sorce et al. (2014).

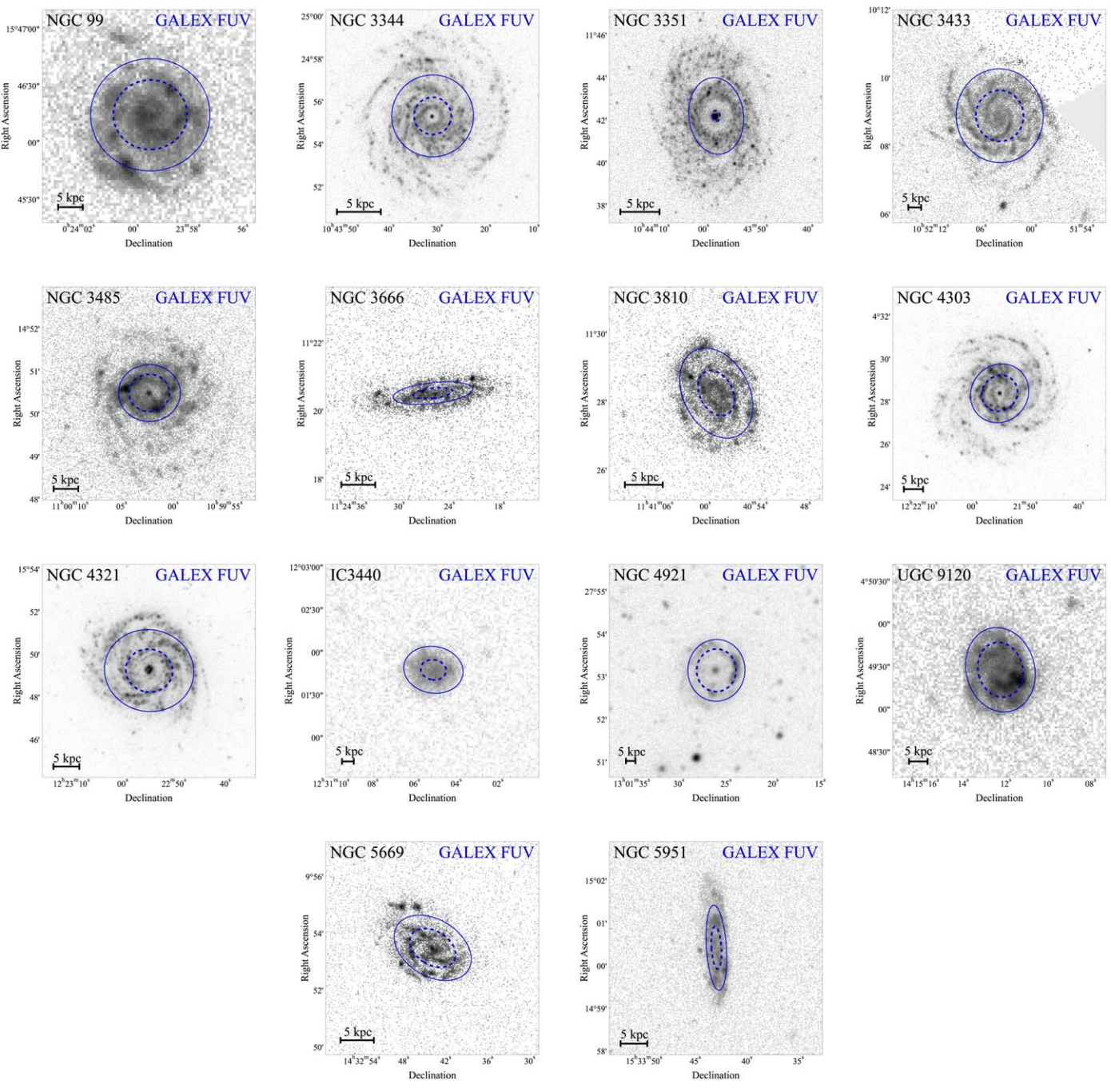


Figure 1. GALEX FUV imagery for our galaxies. The blue ellipses mark the apertures containing 50% (dashed) and 90% (solid) of the total SFR estimated from the combination of FUV and infrared (24 μ m or 22 μ m) maps (see Sections 3 and 4.3 for details). A physical scale of 5.0 kpc is shown at the bottom left corner of each map.

wavelength range from 1140 to 1430 Å in the observed frame. Data reduction and calibration were performed following the standard COS pipeline and the procedures described in the COS Data Handbook (Rafelski et al. 2018). The data covered multiple line transitions including H I λ 1215 (Ly α), Si II $\lambda\lambda$ 1190, 1193, 1260, Si III λ 1206, Si IV $\lambda\lambda$ 1393, 1402, and C II λ 1334. Procedures detailing the absorption line fitting are discussed in S. Borthakur et al. (2024, in preparation).

In this work, we mainly focus on the Ly α absorption line, tracing the neutral hydrogen content of the CGM. In general, absorption line strengths are found to strongly correlate with

the distance of the QSO sightline from the galaxy's optical center, i.e., the impact parameter (Chen et al. 1998). The impact parameters, ρ , for our sightlines range from 26 to 163 kpc. Therefore, before making any comparison between the CGM properties and the galaxies, we normalize the observed equivalent width $(W_{\rm Ly\alpha})$ to that predicted for the same ρ . The predicted equivalent width is estimated by the best-fit line relating the equivalent width and normalized impact parameter, $\rho/R_{\rm vir}$, derived by Borthakur et al. (2016) for the combined sample of COS–Halos and COS–GASS surveys spanning a stellar mass range of $\sim 10^{10-11}\,M_{\odot}$. We adopt the ρ -corrected equivalent width defined as the ratio of the observed equivalent

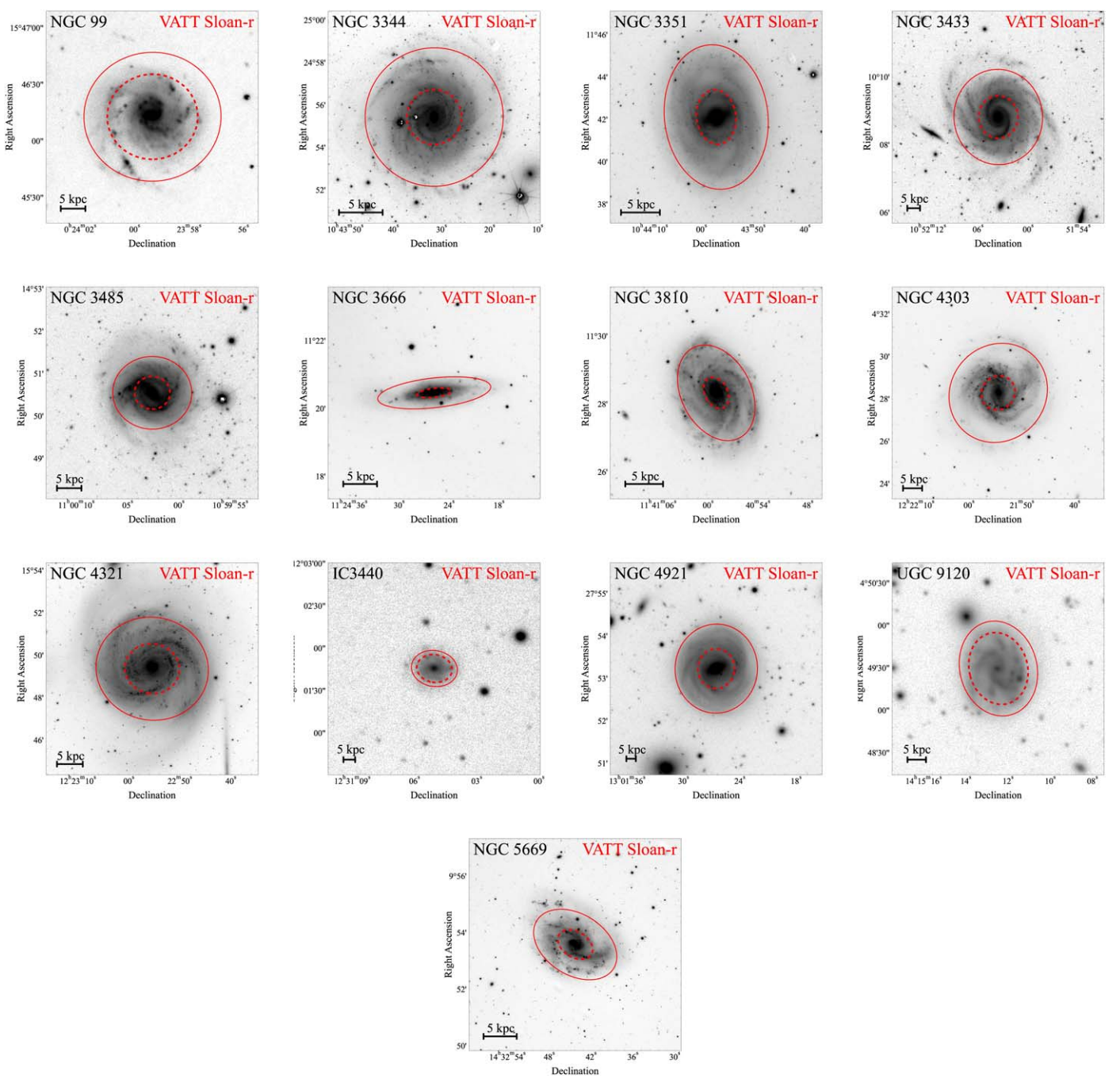


Figure 2. Optical (Sloan-r) imagery of our galaxies. The red ellipses mark the apertures containing 50% (dashed) and 90% (solid) of the total M_{\star} (see Sections 3 and 4.3 for details). A physical scale of 5.0 kpc is shown at the bottom left corner of each map.

width to the predicted equivalent width $(\overline{W}_{{\rm Ly}\alpha})$, also termed the $W_{{\rm Ly}\alpha}$ excess. The impact parameters along with the $W_{{\rm Ly}\alpha}$ excess values are tabulated in Table 1.

3. Derived Galaxy Properties

We derive the SFR surface density, $\Sigma_{\rm SFR}$, from the FUV and 24 $\mu{\rm m}$ maps using the following prescriptions (Salim et al. 2007; Calzetti et al. 2007; Leroy et al. 2008):

$$\Sigma_{\rm SFR}(\rm FUV) = 0.17 I_{\rm FUV} \tag{1}$$

$$\Sigma_{\rm SFR}({\rm FUV} + 24\mu{\rm m}) = 0.081 I_{\rm FUV} + 0.0032 I_{24}$$
 (2)

where $\Sigma_{\rm SFR}$ has units of M_{\odot} yr⁻¹ kpc⁻² and $I_{\rm FUV}$ and $I_{\rm 24}$ are in units of MJy sr⁻¹. Equations (1) and (2) assume a Salpeter (1955) and a Kroupa (2001) initial mass function (IMF), respectively. Equation (1) is divided by factor of 1.59 to correct for the IMF when comparing the values from the above prescriptions. The FUV flux, stemming from the photospheres of massive O and B stars, traces recent star formation (Kennicutt 1998) while the 24 μ m flux density accounts for the dust-processed UV photons. For galaxies without 24 μ m data, the dust-corrected $\Sigma_{\rm SFR}$ is estimated using 22 μ m flux instead of 24 μ m. This may cause the inferred SFRs to be slightly lower but comparable to SFRs estimated using

 Table 2

 VLA Observations and Properties of the Resulting H I Image Cubes

Galaxy	Project Code	Total Integration (hr)	Flux and Bandpass Calibrator	Phase Calibrator	Synthesized Beam Size (arcsec × arcsec)	Velocity Resolution (km s ⁻¹)	Sensitivity (mJy beam ⁻¹ km s ⁻¹)
NGC 99	19B-183	6.5	3C 48	J2340+1333	50.5 × 47.5	2.2	0.98
NGC 3344	AB 365 ^a	11.87	3C 286	1108+201 1040+123	6.7 × 5.4	10.36	0.19
	20A-125	48		J1021+2159			
NGC 3351	17A-090	6.5	3C 147	J1120+1420	53.0×51.0	3.3	0.70
NGC 3433	17A-090	6.5	3C 147	J1120+1420	65.5×51.0	3.3	0.65
NGC 3485	18A-006 19B-183	8.5	3C 286	J1120+1420	54.0×54.0	3.3	0.74
NGC 3666	18A-006 19B-183	8.7	3C 286	J1120+1420	60.5×56.5	3.3	0.60
NGC 3810	17A-090 18A-006	6.5	3C 286	J1120+1420	39.5×30.0	3.3	0.63
NGC 4303	19B-183	6	3C 286	J1150-0023	56.0×48.0	3.3	0.70
NGC 4321	18A-006	4	3C 286	J1254+1141	44.0×30.0	3.3	1.30
IC 3440	•••	•••	•••	•••			•••
NGC 4921	17A-090	18.7	3C 286	3C286	31.5×28.0	20.0	0.19
UGC 9120	17A-090	6.5	3C 286	J1419+0628	69.0×57.5	2.2	1.20
NGC 5669	17A-090	14	3C 286	J143222 +095551	62.5×53.0	3.3	0.85
NGC 5951	17A-090	6.5	3C 286	J1520+2016	73.0×50.5	3.3	0.85

Note.

FUV+24 μm (see Casasola et al. 2017, and references therein). Since the 22 μm flux accounts for UV photons reprocessed by dust, FUV+22 μm is a better estimator of the total SFR than FUV alone. We follow the same procedure of combining the FUV and infrared (22 μm or 24 μm) maps as Padave et al. (2021).

The global SFR estimates presented in Table 1 were made by summing over all the pixels belonging to the galaxy in the FUV and the infrared maps and using the dust-corrected $\Sigma_{\rm SFR}$ prescription. We note that for IC 3440, the SFR is estimated using only the FUV map as the galaxy shows no emission in the 22 μ m map. Identification of pixels belonging to a galaxy was done by creating a segmentation map. Each segmentation map was visually inspected to ascertain that any extended or low-surface-brightness features were included. In certain cases, especially for galaxies spanning more than 8' in the sky, an elliptical region (defined by the galaxy's position angle and ellipticity) larger than the detected region was manually defined to include pixels containing diffuse emission from the galaxy. Foreground objects along the line of sight to each galaxy were separately masked.

The stellar mass (M_{\star}) maps for our galaxies were created by using the relationship derived by Yang et al. (2007) for SDSS galaxies:

$$\log\left(\frac{M_{\star}}{h^{-2}M_{\odot}}\right)$$
= -0.406 + 1.097(g - r) - 0.4(M_r - 5 log h - 4.64).

Here, M_r is the absolute magnitude in r and g - r is the color derived from the g and r maps at each pixel. While creating the M_{\star} maps, pixels were masked if g - r > 3 or g - r < -3 mag, as might result from the subtraction of pixels with low signal-

to-noise ratio or pixels containing sources unassociated with the galaxy. We adopt $h = H_0/(100 \,\mathrm{km\,s^{-1}Mpc^{-1}}) = 0.7$. Global estimates of M_\star were made by summing over the pixels belonging to the target galaxy. These estimates were found to be comparable to those from the Two-micron All Sky Survey's K band (Equation (A2) from Muñoz-Mateos et al. 2007), but our images reach outer galaxy regions of lower stellar density.

The surface density of atomic gas, $\Sigma_{\rm HI}$, for our galaxies, was estimated using the velocity-integrated flux density ($I_{\rm tot}$) VLA H I 21 cm maps and the relation from Mullan et al. (2013):

$$\Sigma_{\rm H\,I} = 1.0 \times 10^4 \, \frac{I_{\rm tot}}{A_{\rm beam}} \tag{3}$$

where $I_{\rm tot}$ has units of Jy beam⁻¹ km s⁻¹ with the beam area, $A_{\rm beam}$, expressed in arcsecond² and $\Sigma_{\rm HI}$ in M_{\odot} pc⁻². The total $M_{\rm HI}$ was found by integrating the total flux. However, some galaxies may have diffuse H I in the outskirts which may not be probed by the VLA maps, causing the $M_{\rm HI}$ estimates to be lower limits. Hence, we adopt the single-dish Arecibo Legacy Fast ALFA (ALFALFA; Haynes et al. 2018) survey measurements for estimating global $M_{\rm HI}$. Since IC 3440 has no observations with the VLA, we only have the global $M_{\rm HI}$ measurement and no $\Sigma_{\rm HI}$ distribution.

The measured SFRs, M_{\star} , and $M_{\rm HI}$ for the sample are presented in Table 1. In Figure 3, we show the distribution of our sample with respect to the star formation main sequence of galaxies. The background bins show the M_{\star} -SFR distribution of local galaxies obtained from the MPA-JHU value-added catalog (Kauffmann et al. 2003; Brinchmann et al. 2004; Salim et al. 2007). Most of our galaxies lie within 0.5 dex from the ridge line of the galaxy main sequence from Renzini & Peng

^a VLA archival data (PI: F.H. Briggs).

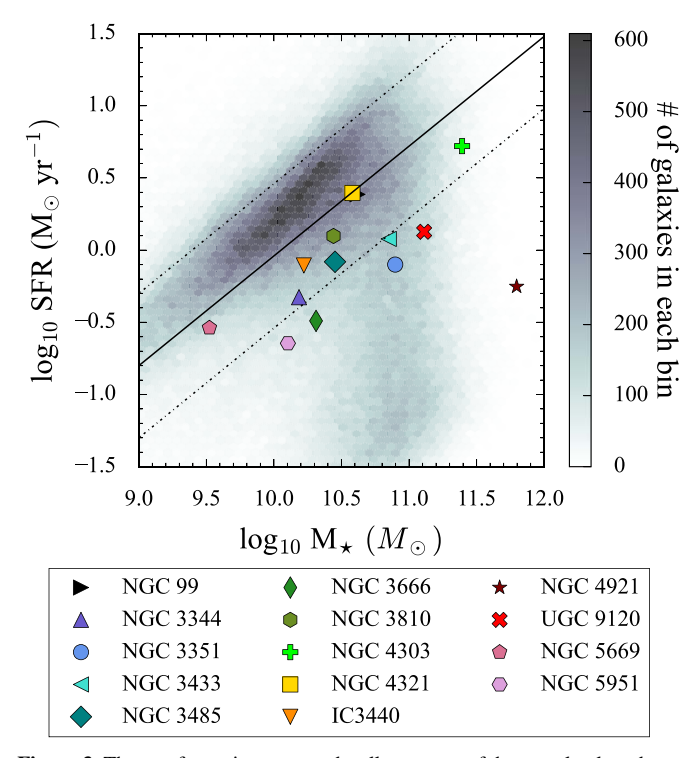


Figure 3. The star formation rates and stellar masses of the sample plotted over the galaxy main sequence obtained from the MPA-JHU value-added catalog. The solid and dashed–dotted lines represent the ridge line of the galaxy main sequence from Renzini & Peng (2015) and ± 0.5 dex from the main sequence, respectively. Each galaxy in the sample has a unique marker that is consistent throughout the paper. Most of our sample galaxies have sSFR $\gtrsim 10^{-11}~\rm yr^{-1}$, with the exception of NGC 4921 with sSFR $< 10^{-11}~\rm yr^{-1}$.

(2015) in the star-forming sequence and the green valley region. Except for NGC 4921, all galaxies have sSFR $\gtrsim 10^{-11} \, \text{yr}^{-1}$ and are considered star-forming. NGC 4921 has sSFR = $10^{-12.0} \, \text{yr}^{-1}$ and is a member of the Coma cluster (Cramer et al. 2021). We note that there could be a discrepancy between our SFR and M_{\star} estimates and those from MPA-JHU. Therefore, the M_{\star} -SFR distribution of local galaxies in Figure 3 is intended only for reference and illustration.

4. Results

4.1. Radial Surface Brightness Profiles

Surface photometry of the panchromatic maps of our galaxies was performed by fitting elliptical isophotes with a fixed center using the IDL routine galprof, 10 where the routine estimates the position angle and ellipticity of the ellipse for each map. Figure 4 shows the surface brightness profiles in FUV, NUV, $g,\,r,\,$ and $22\,\mu\mathrm{m}$ or $24\,\mu\mathrm{m}$. The surface brightnesses in FUV, NUV, $g,\,r,\,$ and $22\,\mu\mathrm{m}$ are estimated in units of mag arcsec $^{-2}$ and the $24\,\mu\mathrm{m}$ flux is estimated in Jy arcsec $^{-2}$. The profiles are extracted until a surface brightness limit of 3σ is reached. Uncertainties in the surface brightness include the Poisson noise in the signal in a given annulus and error in the background subtraction. Disregarding the fluctuations in the inner part (likely caused by the presence of a bulge), we find that all profiles generally drop smoothly with radius. Some also show variations caused by asymmetries in

the flux distribution and the presence of spiral arms. As is evident from the surface brightness profiles, most of the $22 \,\mu\mathrm{m}$ data are dominated by noise. In NGC 4921, a prominent break is observed in the FUV and NUV profiles at $\sim \! 10 \,\mathrm{kpc}$ while the g and r profiles drop smoothly. This upturn in the UV profiles results from the bright star-forming feature in the spiral arm of the galaxy. Following this, the FUV emission shows a steep drop.

We fit an exponential curve to the surface brightness (μ) profiles, $\mu = \mu_0 + 1.086(R/h_{\lambda})$, where μ_0 is the surface brightness at radius R = 0 and h_{λ} is the scale length (de Vaucouleurs 1948). The inner part of the radial profiles, which is dominated by emission from the bulge, was excluded from the fit. This bulge-dominated region was identified by guesstimating the bulge radius from the r-band map, followed by looking for a break in the r-band surface brightness profile near this region. Once we estimate the bulge radius, this value is then adopted for all profiles of a galaxy. Figure 5 shows the h_{λ}/R_{25} measurements in FUV, NUV, g, r, and 24 μ m of our galaxies. The R_{25} values are obtained from a simulated B-band profile created using the g and r profiles and the transformation B = g + 0.33(g - r) + 0.20 from Jester et al. (2005). We do not make any scale length measurements for the 22 μ m maps due to their poor resolution and shallow depths. The estimated R_{25} of the galaxies and h_{λ} values are noted in Table 3. Larger scale lengths imply an extended distribution and smaller values indicate a stronger concentration toward the center. In general, we find decreasing h_{λ} toward longer wavelengths. For most galaxies, $h_{\rm FUV} > h_r$. In particular, in NGC 3433, $h_{\rm FUV}/h_r \gtrsim 2$ indicates that younger stars are twice as extended as older stellar populations. For NGC 4921, $h_{\rm FUV} \approx h_r$, and for NGC 4321, UGC 9120, and NGC 5951, $h_{FUV} < h_r$.

4.2. Radial Profiles of SFR, Stellar Mass, and H I Masss

We also derive the radial profiles of $\Sigma_{\rm SFR}$, Σ_{\star} , and $\Sigma_{\rm HI}$ using the surface brightness profiles and the prescriptions provided in Section 3. Figure 6 shows the radial variation in $\Sigma_{\rm SFR}$, Σ_{\star} , and $\Sigma_{\rm HI}$. The dust-corrected values of $\Sigma_{\rm SFR}$ are systematically higher than the unobscured $\Sigma_{\rm SFR}$ derived from FUV, validating the inclusion of the mid-infrared data. The Σ_{\star} profiles show a smooth decline with radius in all galaxies. The minor variations that come across as breaks in the profile could be due to asymmetries in the galactic structure in the outer parts of galaxies. The $\Sigma_{\rm HI}$ profile is seen to stay relatively flat over the stellar disk, reflecting, to a significant extent, the selection of the sample.

Using these profiles, we are able to derive the radial variations in sSFR (star formation rate per unit stellar mass) and H I-based star formation efficiency (SFE; star formation rate per unit HI mass). Due to the immense variation in the resolution of our H I data, we do not convolve the Σ_{SFR} , Σ_{\star} , and Σ_{HI} profiles to a fixed resolution. Instead, we perform a 1D interpolation on the $\Sigma_{\rm SFR},~\Sigma_{\star},$ and $\Sigma_{\rm HI}$ profiles and then measure the radial gradients in sSFR and SFE. We do not expect this to affect the overall radial gradients due to the overall averaging of fluxes. The sSFR and SFE profiles for our galaxies are estimated using the dust-corrected $\Sigma_{\rm SFR}$ measurements, shown in Figure 7. The sSFR profiles extend as far as the combined range of the Σ_{\star} and $\Sigma_{\rm SFR}$ profiles. In some cases, the discontinuation of Σ_{\star} profiles occurs prior to that of Σ_{SFR} profiles, which is particularly evident in NGC 3666 and IC 3440. Hence, we caution the reader that we are not always

https://www.public.asu.edu/~rjansen/idl/galprof1.0/galprof.pro

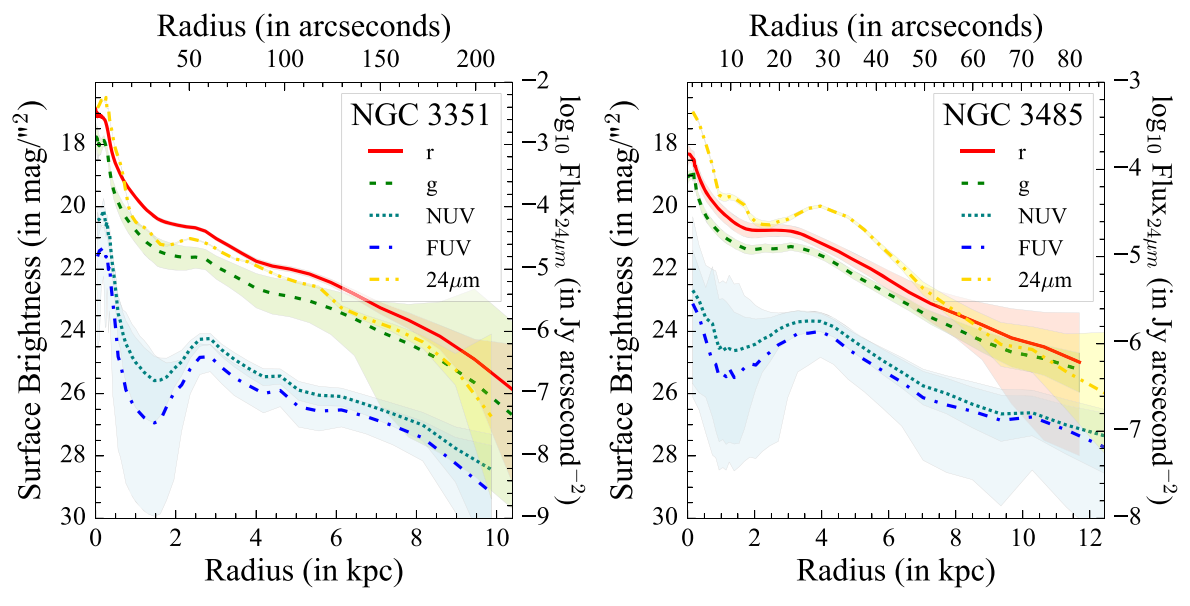


Figure 4. Multiwavelength profiles of surface brightness for the galaxies in our sample. The profiles for r, g, NUV, and FUV are presented in mag arcsec⁻², while the 24 μ m profiles are shown in Jy arcsec⁻². The shaded region around each profile shows the 1σ uncertainty in the surface brightness. The full figure set is available in the electronic version of the paper.

(The complete figure set (14 images) is available.)

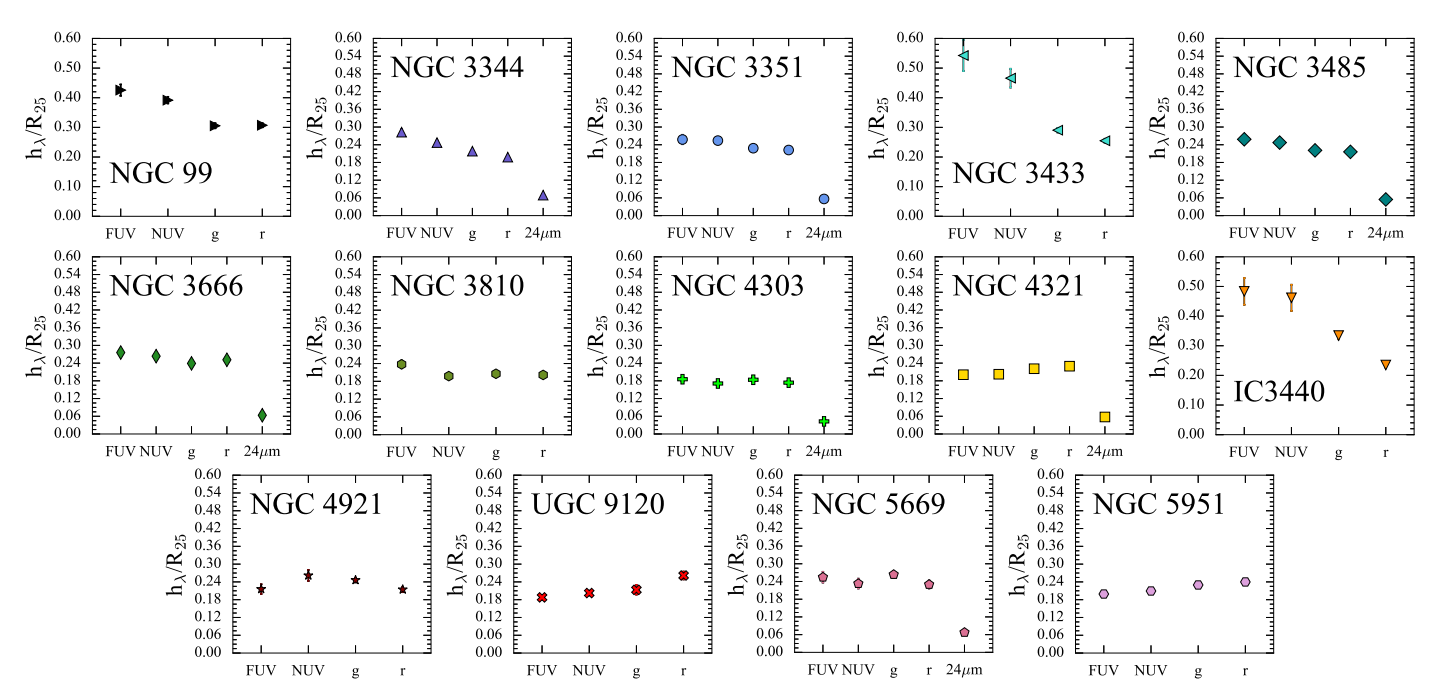


Figure 5. Scale lengths in the FUV, NUV, g, r, and 24 μ m normalized to R_{25} . The scale lengths are obtained by fitting an exponential function to the surface brightness profiles, excluding their central regions.

probing the full extent of the sSFR distribution in these galaxies.

In general, the sSFR profile provides an excellent opportunity to investigate the contributions of young and old stars, and it has been well established that the gradient of the sSFR profile is an indicator of both the growth of the stellar disk and its direction (Muñoz-Mateos et al. 2007). Across our sample, we find that the sSFR profiles exhibit various trends. While NGC 3344, NGC 3433, and IC 3440 show a steady increase in the sSFRs with radius, NGC 4321 shows a steady decline. A positive gradient in the radial profile provides evidence for

inside-out disk growth while a negative gradient could be a result of outside-in formation, affected by the galaxy's environment. The sSFR profile for the remaining galaxies either stays relatively flat or shows pronounced breaks. Along with NGC 4321, a decline in the sSFR profiles is seen in NGC 3666 and UGC 9120, although both galaxies show breaks in their profiles.

The H I-based SFE profiles, however, show a steady drop with galactocentric radii for our galaxies, generally extending as far as $\Sigma_{\rm SFR}$, except for NGC 4921. The decline suggests a radial increase in depletion time ($\tau_{\rm dep} \propto {\rm SFE}^{-1}$), which is the

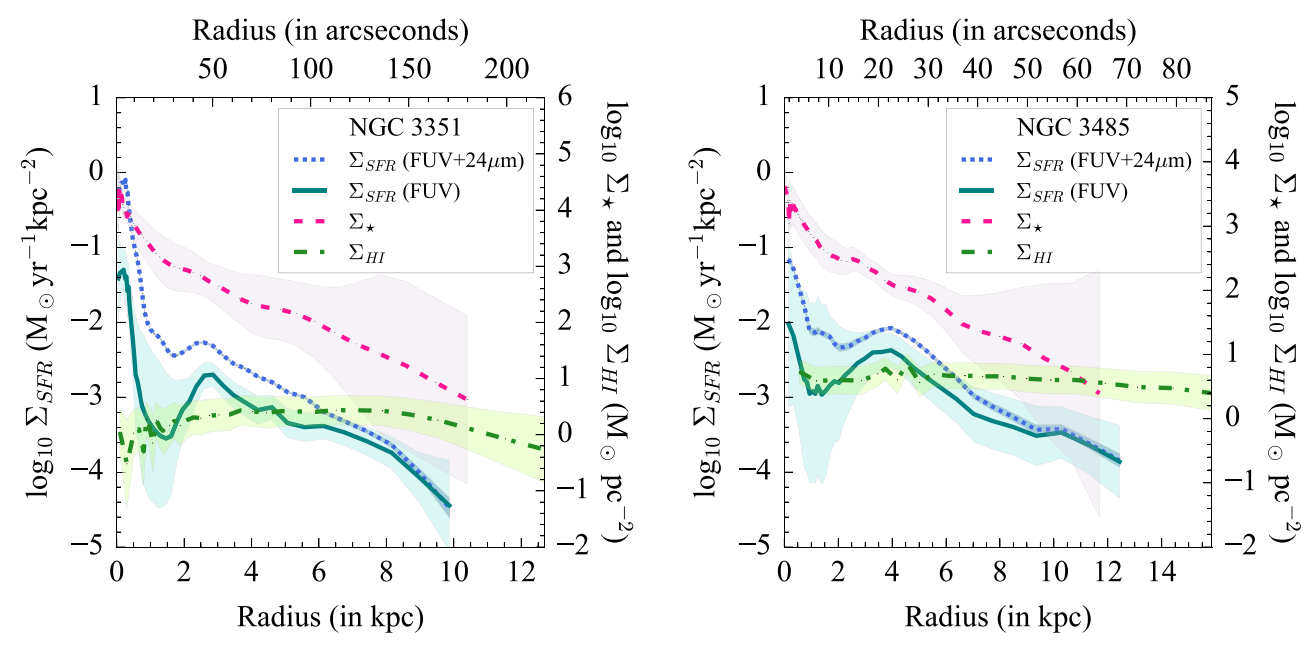


Figure 6. Profiles of Σ_{SFR} obtained from FUV and FUV+24 μ m (or FUV+22 μ m), Σ_{\star} , and Σ_{HI} for the galaxies in our sample. The shaded region around each profile shows the 1σ uncertainty in the respective quantities. The full figure set is available in the electronic version of the paper. (The complete figure set (14 images) is available.)

Table 3 Exponential Scale Lengths, h_{λ} , Expressed in kpc in Different Bands Obtained from the Surface Brightness Profiles

Galaxy	R ₂₅ (kpc)	$h_{ m FUV} \ (m kpc)$	$h_{ m NUV} \ m (kpc)$	$h_g \ m (kpc)$	h_r (kpc)	$h_{24~\mu\mathrm{m}} \ \mathrm{(kpc)}$
NGC 99	11.46	4.88 _{±0.22} (0.99)	$4.49_{\pm0.13}$ (1.0)	$3.5_{\pm0.1}$ (1.0)	$3.52_{\pm0.08}$ (1.0)	
NGC 3344	7.93	$2.24_{\pm 0.08} \ (0.98)$	$1.96_{\pm 0.06} \ (0.98)$	$1.73_{\pm 0.03}$ (1.0)	$1.57_{\pm 0.03}$ (1.0)	$0.55_{\pm 0.02}$ (1.0)
NGC 3351	8.15	$2.1_{\pm 0.13} (0.99)$	$2.07_{\pm 0.09} (0.99)$	$1.86_{\pm0.08}$ (1.0)	$1.81_{\pm 0.07}$ (1.0)	$0.46_{\pm 0.02}$ (1.0)
NGC 3433	17.66	$9.58_{\pm 0.93}$ (0.89)	$8.23_{\pm 0.56}$ (0.99)	$5.13_{\pm0.14}$ (1.0)	$4.5_{\pm 0.12}$ (1.0)	•••
NGC 3485	9.87	$2.55_{\pm 0.16}$ (0.98)	$2.44_{\pm0.14}$ (0.99)	$2.18_{\pm 0.07}$ (1.0)	$2.13_{\pm 0.05}$ (1.0)	$0.54_{\pm 0.02}$ (0.97)
NGC 3666	4.9	$1.35_{\pm 0.06} (0.98)$	$1.29_{\pm 0.04}$ (1.0)	$1.17_{\pm 0.02}$ (1.0)	$1.23_{\pm 0.03}$ (1.0)	$0.31_{\pm 0.01}$ (1.0)
NGC 3810	7.54	$1.79_{\pm 0.1} (0.99)$	$1.49_{\pm 0.07} (0.99)$	$1.55_{\pm 0.07}$ (1.0)	$1.52_{\pm 0.06}$ (1.0)	•••
NGC 4303	17.37	$3.22_{\pm 0.19}$ (1.0)	$2.97_{\pm 0.15}$ (1.0)	$3.19_{\pm 0.09}$ (1.0)	$3.02_{\pm 0.08}$ (1.0)	$0.74_{\pm 0.02}$ (1.0)
NGC 4321	12.85	$2.58_{\pm0.14}$ (0.98)	$2.6_{\pm 0.12} (0.99)$	$2.84_{\pm0.12}$ (1.0)	$2.95_{\pm0.11}$ (1.0)	$0.74_{\pm 0.03}$ (1.0)
IC 3440	11.07	$5.35_{\pm 0.5} (0.97)$	$5.11_{\pm 0.49} (0.99)$	$3.7_{\pm0.14}$ (1.0)	$2.6_{\pm0.1}$ (1.0)	•••
NGC 4921	23.04	$4.97_{\pm0.38}$ (1.0)	$6.03_{\pm 0.43}$ (1.0)	$5.67_{\pm 0.19}$ (1.0)	$4.94_{\pm0.21}$ (1.0)	•••
UGC 9120	10.97	$2.06_{\pm0.08}$ (1.0)	$2.22_{\pm 0.09}$ (0.99)	$2.34_{\pm0.18}$ (0.98)	$2.87_{\pm 0.15}$ (1.0)	
NGC 5669	6.52	$1.66_{\pm 0.12} (0.98)$	$1.52_{\pm 0.11} (0.99)$	$1.72_{\pm 0.08}$ (1.0)	$1.5_{\pm 0.09}$ (1.0)	$0.44_{\pm 0.03}$ (0.98)
NGC 5951	6.88	$1.37_{\pm 0.05}$ (0.98)	$1.44_{\pm 0.05} (0.99)$	$1.58_{\pm 0.02}$ (1.0)	$1.65_{\pm 0.03}$ (1.0)	•••

Note. The Spearman rank correlation coefficient of each fit is noted in parentheses.

time taken by the current rate of star formation to consume the available supply of gas. We note that the peculiarity of the SFE profile of NGC 4921 is a result of its environment. While radial profiles inherently assume a symmetric distribution, the H I disk of NGC 4921 is found to be truncated and asymmetric (Kenney et al. 2015) as a consequence of ram pressure stripping of its ISM due to the dense cluster environment.

We measure the slopes of the sSFR and SFE profiles, $m_{\rm sSFR}$ and $m_{\rm SFE}$, respectively, by fitting a straight line function and excluding the bulge-dominated inner part in the fit. $m_{\rm sSFR}$, $m_{\rm SFE}$, and the intercepts, $b_{\rm sSFR}$ and $b_{\rm SFE}$, of the profiles along with the Spearman's rank correlation coefficient (ρ) are noted in Table 4. For each fit, we find p < 0.001. In Figure 8, we plot $m_{\rm sSFR}$ and $m_{\rm SFE}$ of our galaxies. While the sSFR profiles show both positive and negative gradients, $m_{\rm SFE}$ generally has

negative values, except for NGC 4921. We find a positive relation between the slopes (Spearman's $\rho=0.4$), showing a flattening of the SFE profiles with increasing sSFR gradients. This flattening would suggest an almost constant $\tau_{\rm dep}$ in galaxy disks exhibiting a higher ratio of young to old stars in their outer parts. However, the slopes show a large scatter, and the trend is observed to be statistically insignificant (p>0.1).

Assuming the trend in Figure 8 to be plausible, we could speculate that if galaxies stabilize their H I consumption and maintain a constant $\tau_{\rm dep}$, their star formation then is likely proceeding in the outward direction, i.e., the galaxies are evolving inside-out. In nearby spiral galaxies, molecular gas shows a constant $\tau_{\rm dep} \sim 2$ Gyr (Leroy et al. 2008; Bigiel et al. 2011), highlighting the importance of H₂ for star formation. The H I SFEs, however, tend to be significantly lower in the

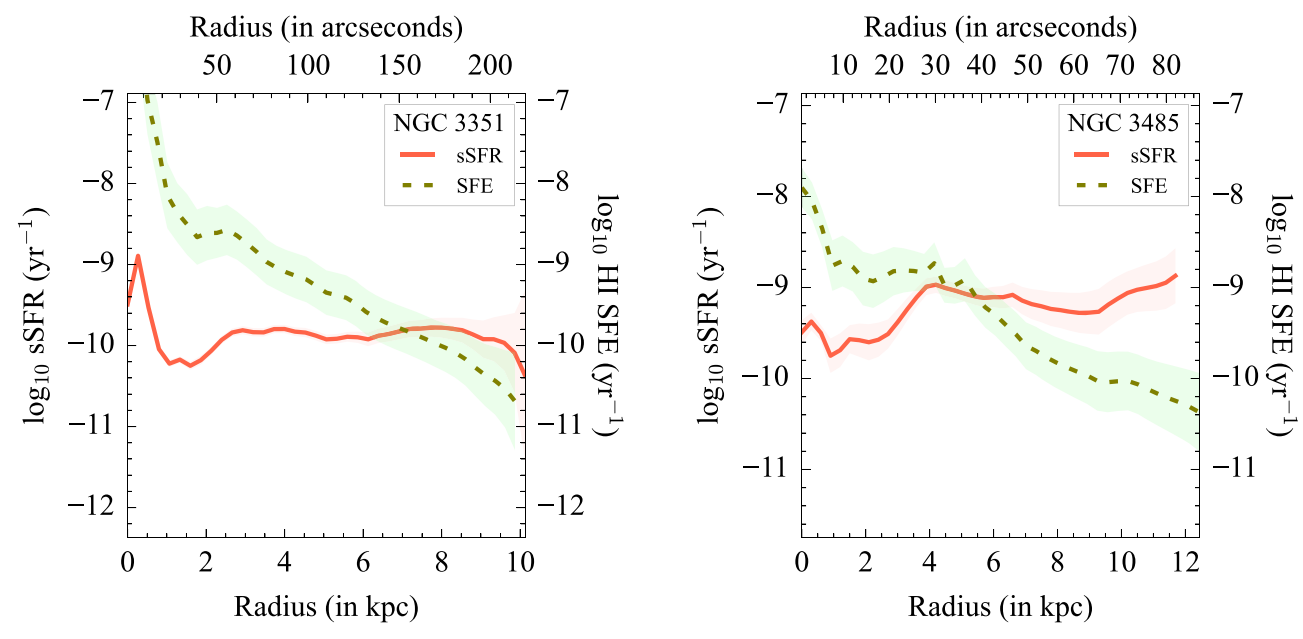


Figure 7. Radial variation in specific SFR and H I star formation efficiency for the galaxies in our sample. The shaded region around each profile shows the 1σ uncertainty in the respective quantities. The full figure set is available in the electronic version of the paper. (The complete figure set (14 images) is available.)

Table 4 Slopes, m, Intercepts, b, and the Spearman rank correlation coefficient (ρ) for each fit of the sSFR and SFE

Galaxy	$m_{ m sSFR}$	$b_{ m sSFR}$	Spearman's ρ	$m_{ m SFE}$	$b_{ m SFE}$	Spearman's ρ
NGC 99	$0.025_{\pm 0.0003}$	$-9.082_{\pm 0.003}$	0.54	$-0.057_{\pm 0.0003}$	$-8.443_{\pm 0.003}$	-0.77
NGC 3344	$0.112_{\pm 0.0004}$	$-9.684_{\pm0.003}$	0.94	$-0.198_{\pm 0.0004}$	$-8.63_{\pm0.003}$	-0.98
NGC 3351	$-0.008_{\pm 0.0003}$	$-9.806_{\pm0.002}$	-0.16	$-0.258_{\pm 0.0002}$	$-7.999_{\pm 0.002}$	-0.99
NGC 3433	$0.107_{\pm 0.0001}$	$-10.095_{\pm 0.002}$	0.99	$-0.045_{\pm 0.0001}$	$-8.939_{\pm0.001}$	-0.99
NGC 3485	$0.004_{\pm 0.0005}$	$-9.147_{\pm 0.004}$	0.06	$-0.186_{\pm0.0004}$	$-8.181_{\pm 0.003}$	-0.99
NGC 3666	$-0.189_{\pm 0.0013}$	$-9.066_{\pm0.007}$	-0.76	$-0.247_{\pm 0.0008}$	$-8.968_{\pm 0.005}$	-0.99
NGC 3810	$0.005_{\pm 0.0006}$	$-8.96_{\pm0.003}$	0.21	$-0.244_{\pm 0.0005}$	$-8.137_{\pm 0.004}$	-0.99
NGC 4303	$-0.003_{\pm 0.0003}$	$-9.235_{\pm 0.003}$	-0.12	$-0.131_{\pm 0.0002}$	$-7.972_{\pm 0.003}$	-0.99
NGC 4321	$-0.061_{\pm 0.0001}$	$-8.525_{\pm0.001}$	-0.97	$-0.111_{\pm 0.0003}$	$-8.277_{\pm 0.003}$	-0.93
IC 3440	$0.397_{\pm 0.001}$	$-9.95_{\pm 0.005}$	0.99	$-0.089_{\pm 0.0002}$	$-9.054_{\pm 0.001}$	-0.99
NGC 4921	$0.075_{\pm 0.0003}$	$-11.726_{\pm0.007}$	0.78	$0.01_{\pm 0.0002}$	$-8.922_{\pm 0.002}$	0.48
UGC 9120	$-0.088_{\pm 0.0005}$	$-9.887_{\pm 0.004}$	-0.89	$-0.129_{\pm 0.0002}$	$-8.024_{\pm 0.002}$	-0.99
NGC 5669	$-0.004_{\pm 0.0012}$	$-8.862_{\pm 0.007}$	-0.13	$-0.206_{\pm 0.0007}$	$-8.865_{\pm0.004}$	-0.97
NGC 5951	$0.063_{\pm 0.0002}$	$-9.45_{\pm 0.001}$	0.99	$-0.162_{\pm 0.0004}$	$-9.045_{\pm 0.002}$	-0.99

outer parts than in the inner parts. This inefficiency is likely being driven by the low molecular gas content in the H I-dominated phase (Leroy et al. 2008; Krumholz et al. 2009; Rafelski et al. 2016). In this regard, Leroy et al. (2008) observed a positive relation between SFE and Σ_{\star} in H I-dominated regions of nearby galaxies. This could imply that stellar potential well/feedback can allow for the conversion of H I to H₂—corroborating our observation in Figure 8 or simply hinting toward the current star formation following past star formation.

4.3. Structural Properties of SFR and Stellar Mass

In the left panel of Figure 9, we show the effective radii of the SFR and M_{\star} maps for the galaxies. The effective radius is defined as the radius that contains 50% of the galaxy's total emission for a particular wavelength or band. In our case, we define $R_{\rm eff,SFR}$ and $R_{\rm eff,M_{\star}}$ as the effective radii of the SFR and M_{\star} maps, respectively. $R_{\rm eff,SFR}$ and $R_{\rm eff,M_{\star}}$ are also shown in

Figures 1 and 2, respectively, as the dashed elliptical apertures marking the area containing 50% of the galaxy's total SFR and M_{\star} . The values are noted in Table 5.

In general, galaxies with $R_{\text{eff,SFR}} > R_{\text{eff},M_{\star}}$ should have an extended star formation distribution, indicating that growth is propagating outwards. However, effective radii are susceptible to intrinsic factors affecting star formation and its measurement. This can be seen as the larger deviations of galaxies from the one-to-one line toward the $R_{\text{eff},M_{\star}}$ side in Figure 9 while the ones with an extended SFR distribution show $R_{\rm eff,SFR} \lesssim$ $1.5 \times R_{\text{eff},M_{\star}}$. This is most likely a result of estimating $R_{\text{eff,SFR}}$ from the dust-corrected SFR maps. Dust, which is concentrated in the center, adds a significant contribution to the SFR in the inner parts of the galaxy, reducing $R_{\text{eff,SFR}}$. A concentrated SFR distribution could also result from starburst activity in the center. The lower $R_{\rm eff,SFR}$ in NGC 3351 is the consequence of bar-driven stellar activity in the circumnuclear region (Colina et al. 1997; Hägele et al. 2007; Leaman et al. 2019). In such cases, information on what is happening at large radii can be

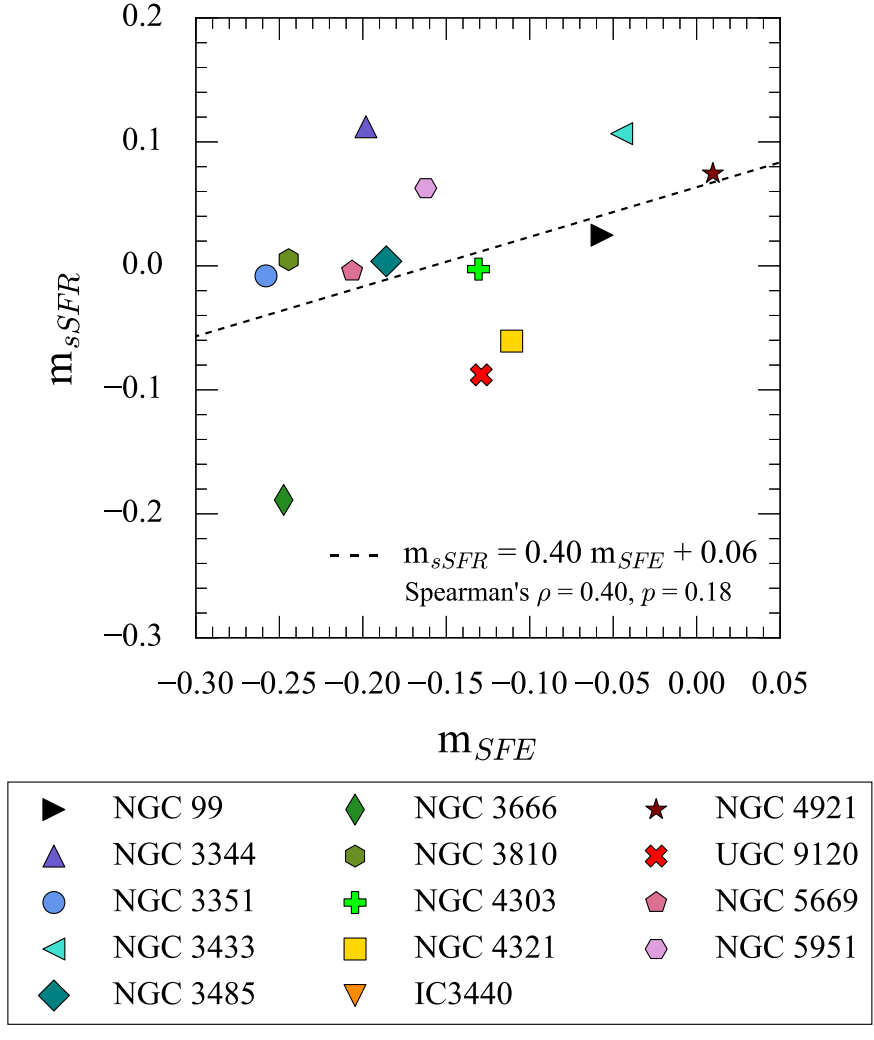


Figure 8. Slopes of the sSFR ($m_{\rm SSFR}$) and SFE ($m_{\rm SSFE}$) profiles for the galaxies. The slopes are estimated by fitting a straight line to the corresponding radial profiles, excluding the bulge. The dashed line represents the line of best fit to the points. The equation defining the best-fit line is noted in the panel. The observed positive correlation links the direction of disk growth to the cold gas in the ISM and how efficiently it is being used to form stars.

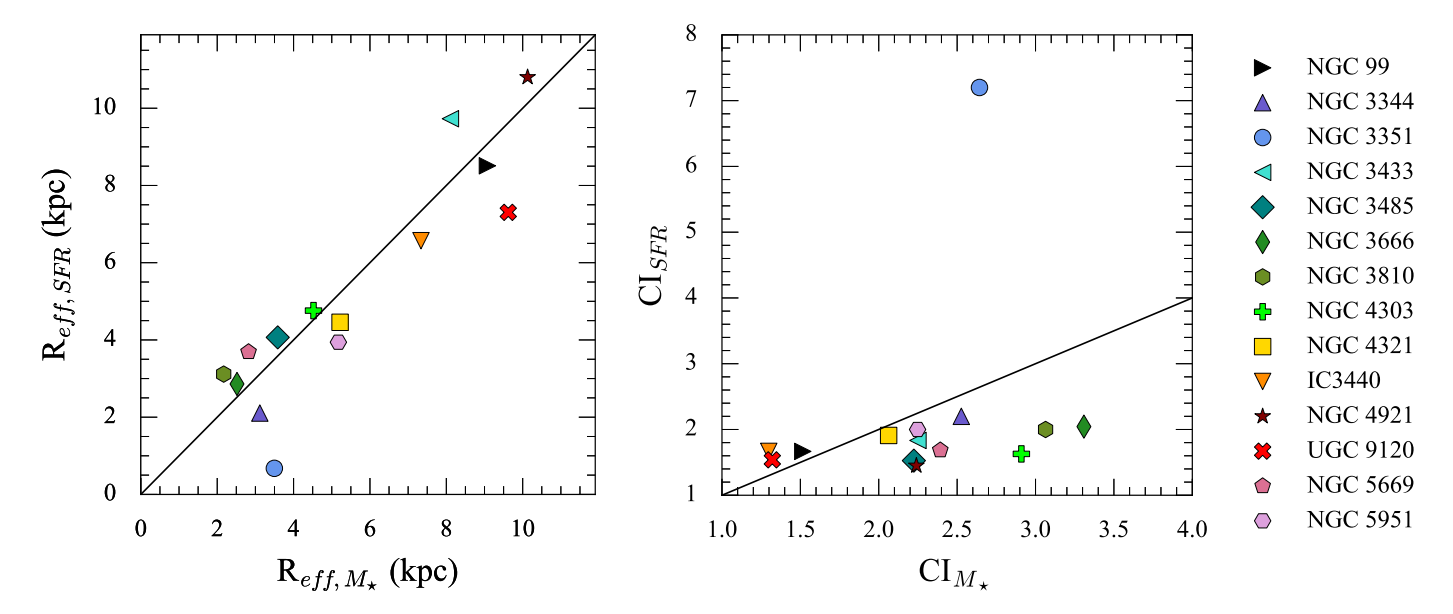


Figure 9. Effective radii, $R_{\rm eff}$ (or R_{50} , left) and the concentration index (CI = R_{90}/R_{50} , right) of SFR and M_{\star} distributions for our galaxies. The black solid line denotes a one-to-one correspondence between the quantities. The majority of the galaxies show ${\rm CI}_{\rm SFR} < {\rm CI}_{M_{\star}}$, indicative of star formation activity that is more spread out than the stellar mass already in place.

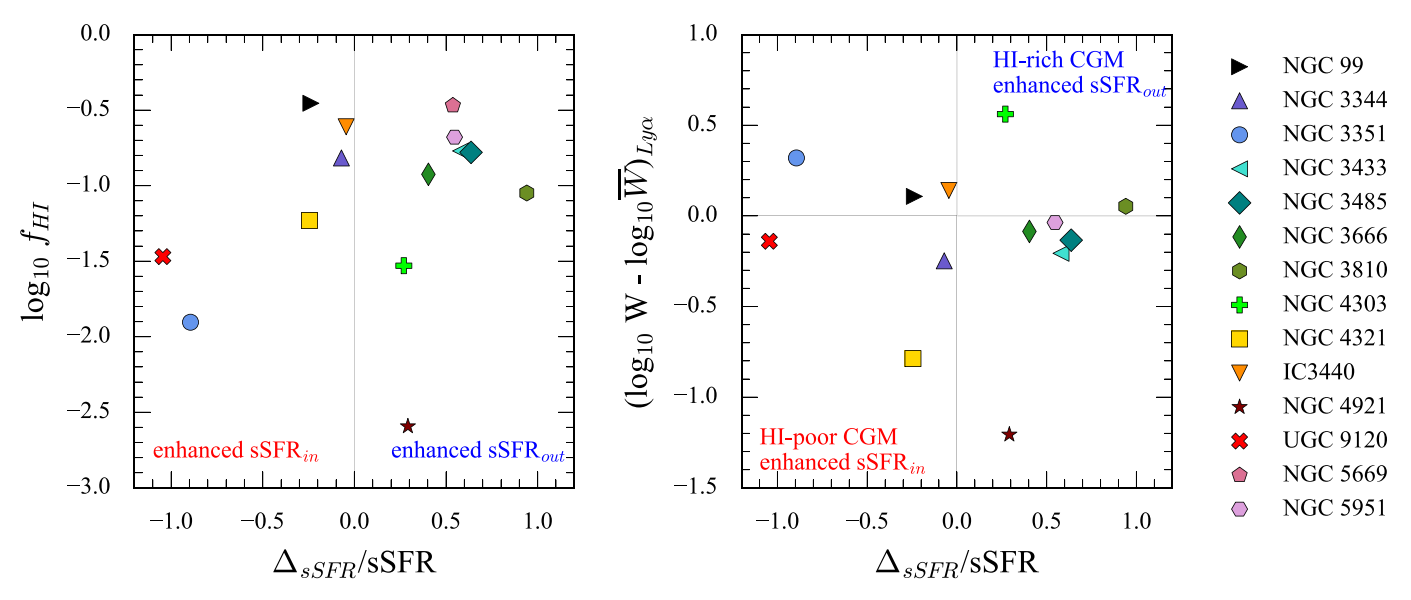


Figure 10. The H I gas fractions (left) and $W_{\rm Ly\alpha}$ excess (right) for the galaxies plotted as a function of $\Delta_{\rm sSFR}/{\rm sSFR}$. The solid lines denote $\Delta_{\rm sSFR}=0$ and $\log_{10}W=\log_{10}\overline{W}$.

Table 5	
Measured Parameters for the Sample Galaxie	s

Galaxy	R _{eff,SFR} (kpc)	$R_{{ m eff},M_{\star}} \ m (kpc)$	CI_{SFR}	$\text{CI}_{M_{\star}}$	$\log_{10}(sSFR_{in}/yr^{-1})$	$log_{10}(sSFR_{out}/yr^{-1})$	d _{NN1} (Mpc)	$d_{\mathrm{NN}_{5}}$ (Mpc)
(1)	(2)	(3)	(4)	(5)	(6)	(7)	(8)	(9)
NGC 99	8.51	9.08	1.67	1.52	-10.18	-10.29	0.56	1.27
NGC 3344	2.11	3.12	2.20	2.53	-10.5	-10.53	0.81	2.07
NGC 3351	0.68	3.50	7.20	2.64	-10.84	-11.26	0.13	1.46
NGC 3433	9.73	8.11	1.83	2.25	-10.92	-10.66	0.85	2.77
NGC 3485	4.07	3.58	1.52	2.22	-10.7	-10.41	1.08	1.35
NGC 3666	2.86	2.52	2.04	3.31	-10.9	-10.72	0.37	1.15
NGC 3810	3.12	2.17	2.00	3.06	-10.62	-10.18	0.57	1.58
NGC 4303	4.76	4.52	1.63	2.91	-10.74	-10.62	0.19	0.56
NGC 4321	4.46	5.22	1.91	2.06	-10.13	-10.24	0.03	0.42
IC 3440	6.57	7.34	1.67	1.30	-10.47	-10.60	0.76	1.44
NGC 4921	10.80	10.13	1.45	2.24	-12.12	-11.99	0.06	0.38
UGC 9120	7.3	9.62	1.54	1.32	-10.8	-11.31	0.07	2.01
NGC 5669	3.69	2.82	1.69	2.40	-10.2	-9.96	0.91	1.85
NGC 5951	3.94	5.17	2.00	2.25	-10.89	-10.64	0.12	1.31

Note. Column (1): galaxies in our sample. Columns (2) and (3): effective radii of the SFR and M_{\star} maps expressed in kpc and described in Section 4.3. Columns (4) and (5): concentration indices of the SFR and M_{\star} maps described in Section 4.3. Columns (6) and (7): sSFR estimated inside and outside $R_{\rm eff,M_{\star}}$, which is used to estimate $\Delta_{\rm sSFR}$ presented in Section 5. Columns (8) and (9): distance to the first and fifth nearest neighbors of the target galaxy expressed in Mpc and described in Section 5.2.

lost in the $R_{\rm eff,SFR}$ – $R_{\rm eff,M_{\star}}$ measurements. Galaxies can still be actively forming stars in the outer regions, albeit at low levels, and not make a dominant contribution to the global SFR. For example, in the left panel of Figure 9, NGC 3344 is seen to have $R_{\rm eff,SFR}$ < $R_{\rm eff,M_{\star}}$. However, the galaxy hosts an XUV disk that accounts for $\lesssim 15\%$ of the total SFR (Padave et al. 2021).

To get a clear picture of the structure in SFR and M_{\star} at large radii, we examine the concentration indices of the respective maps in the right panel of Figure 9. The concentration index (CI) is measured as the ratio of radii containing 90% and 50% of the galaxy's total SFR or M_{\star} . Elliptical apertures containing 90% of a galaxy's total SFR and M_{\star} are marked in Figures 1 and 2, respectively. The concentration indices are also noted in Table 5. Interestingly, the values of CI_{SFR} are quite similar for

our galaxies and show less variation than $\text{CI}_{M_{\star}}$, demonstrating that star formation is generally more extended than the stellar mass distribution for the majority of the sample. We find that most galaxies show $\text{CI}_{M_{\star}} > \text{CI}_{\text{SFR}}$ except NGC 99, NGC 3351, IC 3440, and UGC 9120. The significantly high CI_{SFR} seen in NGC 3351 can be attributed to the central starburst, as discussed earlier.

The extended distribution of young stellar populations traced by the concentration indices, scale lengths, and the radial profiles of $\Sigma_{\rm SFR}$ and M_{\star} provides clues to the direction in which stellar growth may be occurring. While most galaxies in our sample show stellar activity proceeding toward the outer regions, some show signs of outside-in evolution. To investigate further, we quantify stellar disk growth in the next section.

5. Discussion

We have analyzed the SFR, M_{\star} , and H I distributions of 14 low-z galaxies and see stellar growth occurring in the outskirts for most. Following Pezzulli (2021), we quantify the stellar disk growth as $\Delta_{\rm sSFR}/{\rm sSFR}$, where the numerator $\Delta_{\rm sSFR} = {\rm sSFR_{out}} - {\rm sSFR_{in}}$, where ${\rm sSFR_{out}}$ and ${\rm sSFR_{in}}$ are sSFR estimates outside and inside $R_{\text{eff},M_{\star}}$, respectively, and the denominator is the galaxy-integrated sSFR. The inner radius of $R_{\text{eff},M_{\star}}$ essentially divides the galaxy's old stellar population into two equal zones, allowing us to objectively probe star formation activity. Consequently, $\Delta_{sSFR} > 0$ would suggest stellar growth propagating in the outward direction while $\Delta_{\rm sSFR}$ < 0 indicates enhanced SFR in the inner disk and/or suppressed star formation in the outskirts. In our sample, we find that most galaxies show $sSFR_{out} \gtrsim sSFR_{in}$. UGC 9120 shows the lowest value of $\Delta_{\rm sSFR}/{\rm sSFR} \approx -1.04$. Jointly with the negative sSFR gradient, it is likely that this galaxy may be evolving outside-in. We note that the $\Delta_{\rm sSFR}$ measurements can be affected by the active galactic nucleus as it would bias central concentration measurements, and the presence of strong bars in galaxies could alter the sSFR signatures. These were not investigated and lie beyond the scope of this study. The sSFRin and sSFR_{out} values are tabulated in Table 5.

In this section, we will scrutinize how $\Delta_{sSFR}/sSFR$ is associated with cold gas in the ISM and CGM and how stellar growth is affected by a galaxy's environment.

5.1. Connection of Disk Growth with Cold Gas in the ISM and CGM

In the left panel of Figure 10, we show the relation between $\Delta_{\rm sSFR}/{\rm sSFR}$ and the H I gas fraction, $f_{\rm HI}=M_{\rm HI}/(M_{\rm HI}+M_{\star})$. All galaxies have moderate $f_{\rm HI}\gtrsim 0.01$ except for NGC 4921, which has the lowest value of $f_{\rm HI}=2.5\times 10^{-3}$ by virtue of its location in the Coma cluster and stripped ISM. We observe a weak positive correlation (Spearman's $\rho=0.30$) between $\Delta_{\rm sSFR}/{\rm sSFR}$ and $f_{\rm HI}$ for our galaxies with a 1σ scatter of 0.56 dex. Wang et al. (2011) had observed a positive trend between sSFR_{out}/sSFR_{in} and $f_{\rm HI}$ for H I-rich galaxies at 0.025 < z < 0.05 with $M_{\star} > 10^{10} M_{\odot}$. However, this relation was studied for different stellar mass bins and the positive trend differed for each bin. Meanwhile, our sample spans a larger stellar mass range and no binning is performed due to the small size of the sample. The observed scatter is likely a sample selection effect.

While the increase in sSFR with higher f_{HI} is expected (Saintonge & Catinella 2022), a positive correlation between $f_{\rm HI}$ and $\Delta_{\rm sSFR}/{\rm sSFR}$ accentuates the direction in which star formation is likely to propagate. Galaxies with higher $f_{\rm HI}$ tend to have higher ratios of young to old stars in their outskirts—an indication of a rapidly growing outer disk. Besides, a positive correlation can also be thought of as a semblance of the correlation between H I and SFR in the outer parts of a galaxy. In the H I-dominated low-star-forming outer parts, $\Sigma_{\rm HI}$ and $\Sigma_{\rm SFR}$ are known to be correlated (Bigiel et al. 2010; Padave et al. 2021), while the correlation is lacking in the H_2 -dominated inner parts (Bigiel et al. 2008). As a result, $f_{\rm HI}$ would correlate with the outer SFR, and subsequently with $\Delta_{\rm sSFR}/{\rm sSFR}$. Studying a larger sample size may expound on these observed relations, indicating that the increase in the radial sSFR gradient, and thereby the direction of disk growth, can be linked to the cold gas in the ISM and how efficiently it is being used for star formation.

The right panel of Figure 10 shows the $W_{{\rm Ly}\alpha}$ excess, described in Section 2.5, of the detected absorbers in the CGM of our galaxies and disk growth probed by $\Delta_{\rm sSFR}/{\rm sSFR}$. We again bring to the reader's attention that the $W_{{
m Ly}lpha}$ excess takes into account the inhomogeneous radial distribution of the impact parameter in the sample. Our observations show no dependence between $W_{Lv\alpha}$ excess and $\Delta_{sSFR}/sSFR$. Additionally, we also do not see $W_{{
m Ly}lpha}$ excess to show any relation with sSFR and $f_{\rm HI}$ for our galaxies. In general, the $W_{{\rm Ly}\alpha}$ excess is known to strongly correlate with sSFR and $f_{\rm HI}$ (Borthakur et al. 2015, 2016). These were seen for the combined COS-GASS +COS-Halos and COS-GASS samples, respectively. It should be noted that the selection criteria for both the COS-GASS and COS-Halos samples are statistically motivated, probing stellar masses of 10^{10-11} M_{\odot} with redshifts in the ranges $0.05 \gtrsim z \gtrsim 0.025$ and $0.2 \gtrsim z \gtrsim 0.1$, respectively, while the DIISC sample consists of galaxies with known HI disk size and QSO sightlines within $\sim 3.5 \times R_{\rm HI}$, i.e., closer to the disk– halo interface. Hence, the inconsistency between our observation and those from Borthakur et al. (2015, 2016) may not really be a contradiction and can be attributed to a small sample size along with the differences in sample selection. As a result, we infer that the enhancement and suppression of neutral HI gas in the CGM has no effect on the direction in which star formation proceeds in a galactic disk or vice versa.

5.2. Connection of Disk Growth with Environment

The local environment also affects a galaxy's ability to sustain cold gas as well as star formation (Peng et al. 2010, 2015; Muzzin et al. 2012; Darvish et al. 2015, 2016; Steinhauser et al. 2016; Coenda et al. 2019). In this subsection, we investigate how various properties of our galaxies depend on the environment. We make use of the NYU Value-Added Galaxy Catalog (Blanton et al. 2005, NYU-VAGC) derived from SDSS Data Release 7 (Abazajian et al. 2009) to define a magnitude-limited sample of galaxies to study the environment. We consider sources with $M_r \leq -15.97$, which were chosen based on the faintest source in the catalog at the farthest redshift of z = 0.026 in our sample. Subsequently, we search for the nearest neighbors to our galaxies that have relative velocities $|v_{\text{neighbor}} - v_{\text{galaxy}}| \leq 300 \text{ km s}^{-1}$. We then calculate the galaxy's projected distance to its first and fifth nearest L_{\star} neighbors, d_{NN_1} and d_{NN_5} , respectively. We note d_{NN_1} and d_{NN_5}

In the left panel of Figure 11, we find the sSFR to increase with increasing $d_{\rm NN_I}$ for our galaxies (Spearman's $\rho=0.43$). We also see a positive correlation between $\Delta_{\rm sSFR}/{\rm sSFR}$ and $d_{\rm NN_I}$ (top right panel of Figure 11), although with more scatter. These observations suggest that an isolated galaxy is more likely to build its stellar content in an inside-out fashion. Interestingly, this is corroborated by the even tighter correlation between $f_{\rm HI}$ and $d_{\rm NN_I}$, highlighting that these galaxies are able to sustain their cold gas reservoir in sparse environments, which in turn allows them to form stars. The correlations of sSFR, $\Delta_{\rm sSFR}/{\rm sSFR}$, and $f_{\rm HI}$ with $d_{\rm NN_I}$ are tighter than those with $d_{\rm NN_I}$.

In Figure 12, we show the $W_{{\rm Ly}\alpha}$ excess as a function of $d_{{\rm NN_1}}$ and $d_{{\rm NN_5}}$. We find that excluding NGC 4321 and NGC 4921, we see a steady decline in $W_{{\rm Ly}\alpha}$ excess with increasing $d_{{\rm NN_1}}$ and $d_{{\rm NN_5}}$, the anticorrelation quantified with Spearman's ρ of

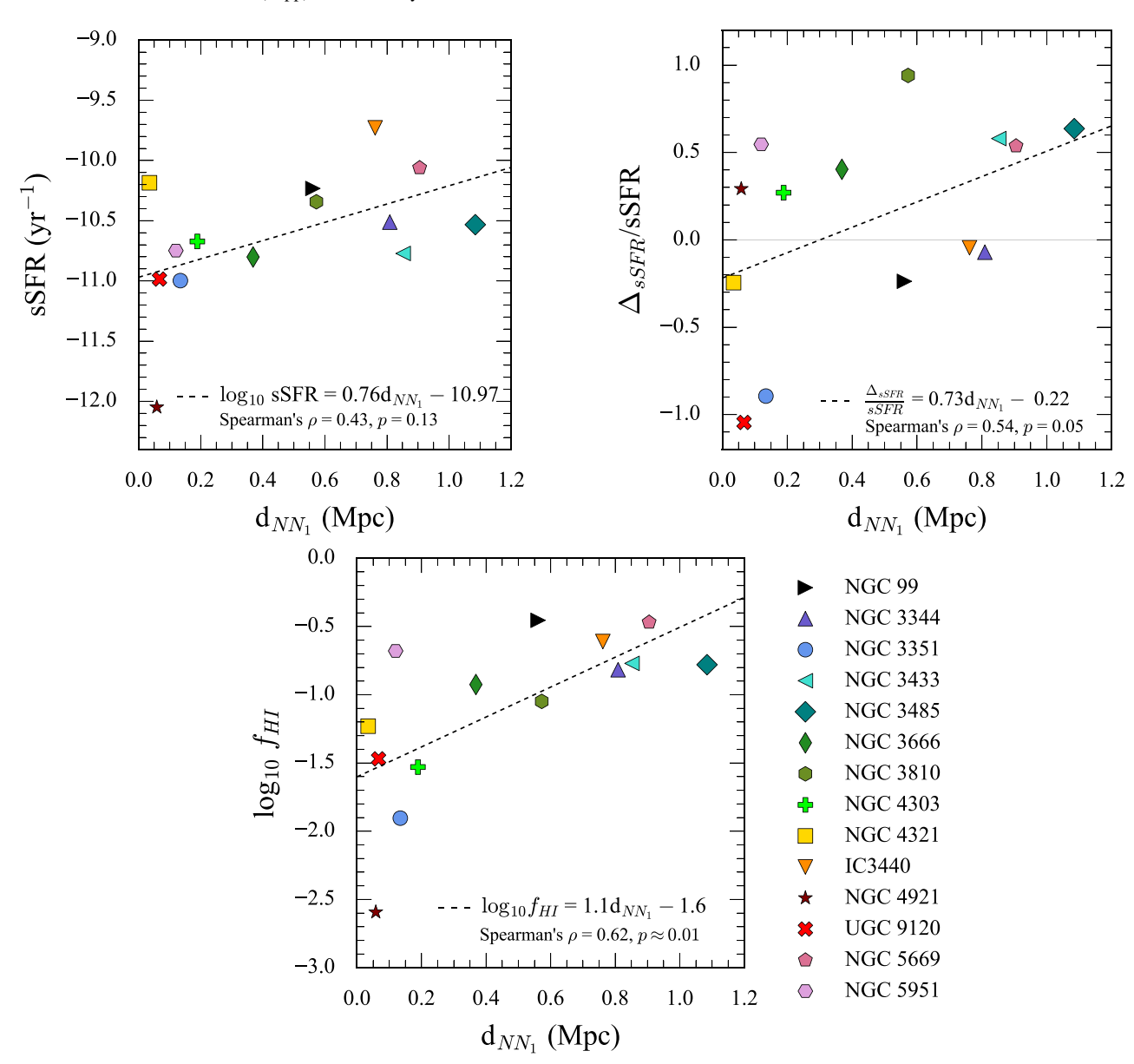


Figure 11. The sSFR (top left), $\Delta_{\rm sSFR}/{\rm sSFR}$ (top right), and H I gas fractions (bottom) as a function of the galaxy's distance from the first nearest neighbor, $d_{\rm NN_I}$. The solid gray line denotes $\Delta_{\rm sSFR}=0$. The lines of best fit for the plots are shown as black dashed lines. Parameters describing the best-fit lines are noted in the plots.

-0.36 and -0.62, respectively. This anticorrelation indicates the suppression of the CGM HI content in isolated environments. While $d_{\rm NN_1}$ simply depicts how far the closest L_{\star} neighbor is from our galaxy of interest, $d_{\rm NN_5}$ can trace the density of the local environment. A shorter d_{NN_5} indicates a denser environment. So, the stronger anticorrelation of $W_{Ly\alpha}$ excess with $d_{\rm NN_5}$ likely indicates that the suppression of $W_{\rm Ly\alpha}$ in the CGM is more affected by the density of the local environment than by the presence of close neighbors. However, the suppression of $W_{\rm Ly\alpha}$ could also result from galaxies undergoing ram pressure stripping (Abadi et al. 1999; Steinhauser et al. 2016; Coenda et al. 2019), causing them to lose their cold gas or strangulate (Peng et al. 2015). NGC 4321 and NGC 4921 show a strong suppression of Ly α in their CGM, likely due to their location in the Virgo and Coma clusters, respectively. In contrast, NGC 4303 and IC 3440 also reside in the Virgo cluster but NGC 4303 possesses abundant H I in its CGM. Yoon & Putman (2013)'s investigation of the background quasars in and around the Virgo cluster showed that the CGM covering fractions of the Ly α absorbers are lower for the Virgo galaxies, indicating that galaxies in the denser environment have suppressed CGM, compared to circumcluster and field galaxies with an abundant CGM. Additionally, NGC 4321's interaction with its companion, NGC 4322, could have also resulted in the suppression of Ly α . The highly suppressed CGM in M100 is suggestive of the galaxy making its way to the red sequence (Gim et al. 2021).

We note that DIISC galaxies, being rich in H I, are likely to be found in a gas-rich large-scale environment (Bortha-kur 2022). Also, galaxy density in the vicinity might play a critical role in dictating the neutral gas content of the CGM and the prevalence of star formation. Further investigation using a larger sample is recommended.

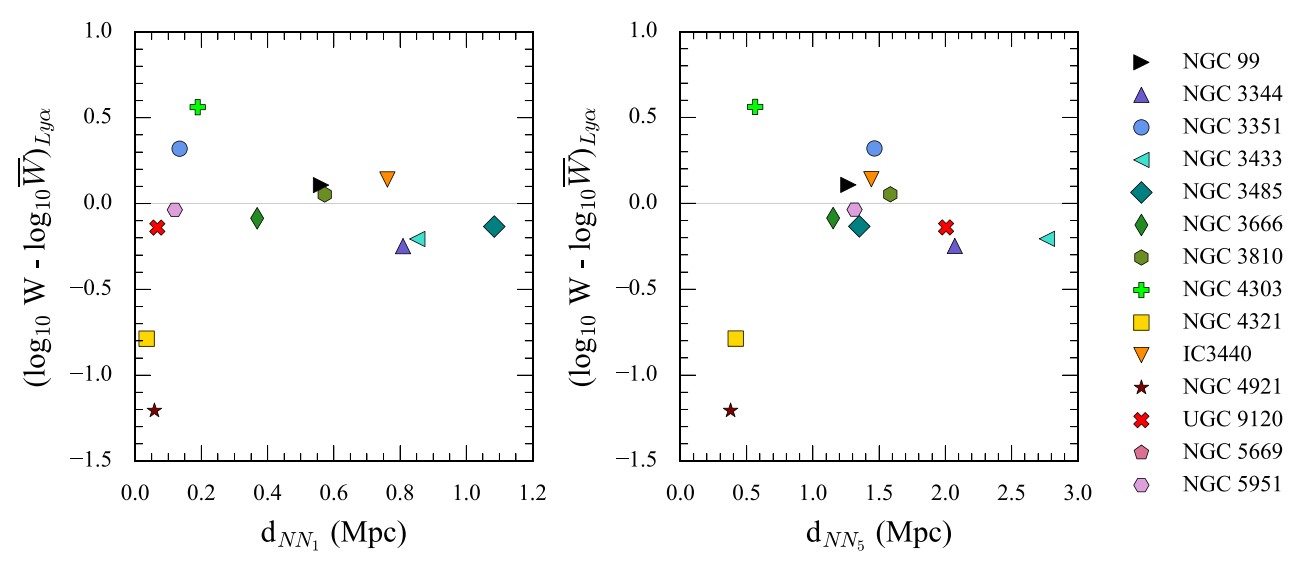


Figure 12. The $W_{\text{Ly}\alpha}$ excess as a function of the galaxy's distance from the first and fifth nearest neighbors, d_{NN_1} (left) and d_{NN_5} (right), respectively. The gray solid line denotes $\log_{10} W = \log_{10} \bar{W}$.

6. Conclusions

In this work, we investigate the radial profiles and distribution of star formation, stellar mass, and H I mass in 14 nearby galaxies and look for clues to disk growth and stellar build-up. We quantify growth as $\Delta_{\rm sSFR}/\rm sSFR$, where $\Delta_{\rm sSFR}=\rm sSFR_{\rm out}-\rm sSFR_{\rm in}$, where sSFR_{\rm out} and sSFR_in are sSFR outside and inside the effective radius of the stellar mass map, and this allows us to comment on the direction of growth and probe the star formation activity. We investigate the connections of $\Delta_{\rm sSFR}/\rm sSFR$ with the atomic gas in the ISM and CGM and the local environment. We summarize our findings below.

- 1. The FUV surface brightness profiles are more extended than those of the r band for most galaxies, as indicated by their exponential scale lengths. About 70% of our galaxies also show $\text{CI}_{\text{SFR}} < \text{CI}_{M_{\star}}$, indicative of an actively star-forming outer disk.
- 2. We find the sSFR profiles exhibit both increasing and decreasing behavior as a function of galactocentric radius, the increase pointing toward an inside-out growing disk. The sSFR gradients show a positive relation (Spearman $\rho=0.4$) with the H I SFE gradients. A bolder interpretation of this observation could be that galaxies are likely to evolve inside-out if they can stabilize their H I consumption rate to maintain constant $\tau_{\rm dep}$ over their disk.
- 3. A positive correlation between $\Delta_{\rm sSFR}/{\rm sSFR}$ and $f_{\rm HI}$ (Spearman $\rho=0.30$) is observed with a 1σ scatter of 0.56 dex. The result highlights the connection of direction of propagation of star formation with H I, indicating an inside-out growth scenario for galaxies with high $f_{\rm HI}$. The atomic gas content in the CGM, probed by $W_{\rm Ly\alpha}$ excess, however, does not show any relation with the direction of stellar growth.
- 4. Both $\Delta_{\rm sSFR}/{\rm sSFR}$ and $f_{\rm HI}$ show a strong positive correlation with the distance to the nearest L_{\star} neighbor, showing that galaxies are able to hold onto their ISM cold gas reservoir in the absence of a close neighbor and subsequently proceed to evolve inside-out.

5. The cold gas content of the CGM probed by $W_{\text{Ly}\alpha}$ excess is seen to be suppressed in dense cluster environments (as expected) but also in isolated environments. The latter is seen as a tight anticorrelation between $W_{\text{Ly}\alpha}$ excess and the distance to the fifth nearest L_{\star} neighbor with Spearman ρ of -0.62. Interestingly, the suppression is affected more by the density of the local environment than the presence of a close neighbor.

Our study sheds light on how environment, and H I in the CGM and ISM affect the stellar growth and evolution of a galaxy. Our results imply that the direction in which stellar growth occurs is likely governed by the distribution of H I and M_{\star} of the galaxy, while the environment controls the cold gas content. In isolated environments, galaxies are likely to evolve inside-out as they are able to sustain their cold gas content in the ISM, which in turn is fed by the CGM via accretion.

As galaxies form new stars at larger radii, subsequent stellar age gradients also arise in that direction. In the future, we will be investigating the age and metallicity gradients and star formation histories for these galaxies with deep, multiband optical imaging. We will investigate the properties of the nearest neighbors to further explore the role the environment plays in controlling the gas content in the ISM and CGM.

Acknowledgments

M.P., S.B., R.J., and D.T. are supported by NASA ADAP grant 80NSSC21K0643, S.B. and H.G. are also supported by NSF Award Number 2009409, and S.B., H.G., and T.H. are supported by HST grant HST-GO-14071 administrated by STScI, which is operated by AURA under contract NAS 5-26555 from NASA.

The Arizona State University authors acknowledge the twenty-three Native Nations that have inhabited this land for centuries. Arizona State University's four campuses are located in the Salt River Valley on ancestral territories of Indigenous peoples, including the Akimel O'odham (Pima) and Pee Posh (Maricopa) Indian Communities, whose care and keeping of these lands allows us to be here today.

We thank the referee for their constructive feedback. We thank the staff at the Space Telescope Science Institute, the National Radio Astronomy Observatory (NRAO) Array Operations Center at Socorro, the Steward Observatory, and the Vatican Advanced Technology Telescope for their help and support on this project. All GALEX and HST data presented in this paper were obtained from the Mikulski Archive for Space Telescopes (MAST) at the Space Telescope Science Institute. The specific observations analyzed can be accessed via 10.17909/rf6m-3y73.

GALEX is a NASA Small Explorer, launched in 2003 April. We gratefully acknowledge NASA's support for the construction, operation, and science analysis of the GALEX mission, developed in cooperation with the Centre National d'Etudes Spatiales (CNES) of France and the Korean Ministry of Science and Technology.

Based on observations made with the NASA/ESA Hubble Space Telescope, obtained from the data archive at the Space Telescope Science Institute. STScI is operated by the Association of Universities for Research in Astronomy, Inc. under NASA contract NAS 5-26555.

This work is also partly based on observations with the VATT: the Alice P. Lennon Telescope and the Thomas J. Bannan Astrophysics Facility.

The National Radio Astronomy Observatory is a facility of the National Science Foundation operated under cooperative agreement by Associated Universities, Inc.

This work is based (in part) on observations made with the Spitzer Space Telescope, which was operated by the Jet Propulsion Laboratory, California Institute of Technology under a contract with NASA.

This publication makes use of data products from the Widefield Infrared Survey Explorer, which is a joint project of the University of California, Los Angeles, and the Jet Propulsion Laboratory/California Institute of Technology, funded by the National Aeronautics and Space Administration.

Facilities: HST, GALEX, Sloan, Spitzer, VATT, VLA, WISE.

ORCID iDs

```
Mansi Padave https://orcid.org/0000-0002-3472-0490
Sanchayeeta Borthakur https://orcid.org/0000-0002-2724-8298
Hansung B. Gim https://orcid.org/0000-0003-1436-7658
David Thilker https://orcid.org/0000-0002-8528-7340
Rolf A. Jansen https://orcid.org/0000-0003-1268-5230
Robert C. Kennicutt https://orcid.org/0000-0001-5448-1821
Andrew J. Fox https://orcid.org/0000-0003-0724-4115
Emmanuel Momjian https://orcid.org/0000-0003-3168-5922
Timothy Heckman https://orcid.org/0000-0001-6670-6370
```

References

```
Abadi, M. G., Moore, B., & Bower, R. G. 1999, MNRAS, 308, 947
Abazajian, K. N., Adelman-McCarthy, J. K., Agüeros, M. A., et al. 2009, ApJS, 182, 543
Avila-Reese, V., González-Samaniego, A., Colín, P., Ibarra-Medel, H., & Rodríguez-Puebla, A. 2018, ApJ, 854, 152
Barden, M., Rix, H.-W., Somerville, R. S., et al. 2005, ApJ, 635, 959
Bell, E. F., & de Jong, R. S. 2000, MNRAS, 312, 497
Bianchi, L., Madore, B., Thilker, D., Gil de Paz, A. & GALEX Science Team 2003, AAS Meeting, 203, 91.12
Bigiel, F., Leroy, A., Seibert, M., et al. 2010, ApJL, 720, L31
```

```
Bigiel, F., Leroy, A., Walter, F., et al. 2008, AJ, 136, 2846
Bigiel, F., Leroy, A. K., Walter, F., et al. 2011, ApJL, 730, L13
Birnboim, Y., & Dekel, A. 2003, MNRAS, 345, 349
Blanton, M. R., Schlegel, D. J., Strauss, M. A., et al. 2005, AJ, 129, 2562
Borthakur, S. 2022, ApJ, 924, 123
Borthakur, S., Heckman, T., Tumlinson, J., et al. 2015, ApJ, 813, 46
Borthakur, S., Heckman, T., Tumlinson, J., et al. 2016, ApJ, 833, 259
Brinchmann, J., Charlot, S., White, S. D. M., et al. 2004, MNRAS, 351, 1151
Brook, C. B., Kawata, D., Martel, H., Gibson, B. K., & Bailin, J. 2006, ApJ,
Brook, C. B., Stinson, G. S., Gibson, B. K., et al. 2012, MNRAS, 426, 690
Brown, T. M., Beaton, R., Chiba, M., et al. 2008, ApJL, 685, L121
Buitrago, F., Trujillo, I., Conselice, C. J., et al. 2008, ApJL, 687, L61
Calzetti, D., Kennicutt, R. C., Engelbracht, C. W., et al. 2007, ApJ, 666, 870
Cardelli, J. A., Clayton, G. C., & Mathis, J. S. 1989, ApJ, 345, 245
CASA Team, Bean, B., Bhatnagar, S., et al. 2022, PASP, 134, 114501
Casasola, V., Cassarà, L. P., Bianchi, S., et al. 2017, A&A, 605, A18
Chen, H.-W., Lanzetta, K. M., Webb, J. K., & Barcons, X. 1998, ApJ, 498, 77
Coenda, V., Mast, D., Martínez, H. J., Muriel, H., & Merchán, M. E. 2019,
     &A, 621, A98
Colina, L., García Vargas, M. L., Mas-Hesse, J. M., Alberdi, A., & Krabbe, A.
   1997, ApJL, 484, L41
Cramer, W. J., Kenney, J. D. P., Tonnesen, S., et al. 2021, ApJ, 921, 22
Dale, D. A., Anderson, K. R., Bran, L. M., et al. 2020, AJ, 159, 195
Dale, D. A., Beltz-Mohrmann, G. D., Egan, A. A., et al. 2016, AJ, 151, 4
Darvish, B., Mobasher, B., Sobral, D., et al. 2016, ApJ, 825, 113
Darvish, B., Mobasher, B., Sobral, D., Scoville, N., & Aragon-Calvo, M. 2015,
    ApJ, 805, 121
de Vaucouleurs, G. 1948, AnAp, 11, 247
Dutton, A. A., van den Bosch, F. C., Faber, S. M., et al. 2011, MNRAS,
   410, 1660
Fall, S. M., & Efstathiou, G. 1980, MNRAS, 193, 189
Ferguson, H. C., Dickinson, M., Giavalisco, M., et al. 2004, ApJL, 600, L107
Frankel, N., Sanders, J., Rix, H.-W., Ting, Y.-S., & Ness, M. 2019, ApJ,
   884, 99
Franx, M., van Dokkum, P. G., Förster Schreiber, N. M., et al. 2008, ApJ,
  688, 770
Gim, H. B., Borthakur, S., Momjian, E., et al. 2021, ApJ, 922, 69
Goddard, D., Thomas, D., Maraston, C., et al. 2017, MNRAS, 466, 4731
Gogarten, S. M., Dalcanton, J. J., Williams, B. F., et al. 2009, ApJ, 691, 115
González Delgado, R. M., Cid Fernandes, R., García-Benito, R., et al. 2014,
   ApJL, 791, L16
Green, J. C., Froning, C. S., Osterman, S., et al. 2012, ApJ, 744, 60
Hägele, G. F., Díaz, Á. I., Cardaci, M. V., Terlevich, E., & Terlevich, R. 2007,
          S, 378, 163
Haynes, M. P., Giovanelli, R., Kent, B. R., et al. 2018, ApJ, 861, 49
Hoeflich, P., Hsiao, E. Y., Ashall, C., et al. 2017, ApJ, 846, 58
Jester, S., Schneider, D. P., Richards, G. T., et al. 2005, AJ, 130, 873
Kauffmann, G., Heckman, T. M., White, S. D. M., et al. 2003, MNRAS,
   341, 33
Kenney, J. D. P., Abramson, A., & Bravo-Alfaro, H. 2015, AJ, 150, 59
Kennicutt, Robert C. J. 1998, ARA&A, 36, 189
Kereš, D., Katz, N., Weinberg, D. H., & Davé, R. 2005, MNRAS, 363, 2
Kourkchi, E., Courtois, H. M., Graziani, R., et al. 2020, AJ, 159, 67
Kroupa, P. 2001, MNRAS, 322, 231
Krumholz, M. R., McKee, C. F., & Tumlinson, J. 2009, ApJ, 693, 216
Laher, R. R., Gorjian, V., Rebull, L. M., et al. 2012, PASP, 124, 737
Larson, R. B. 1976, MNRAS, 176, 31
Leaman, R., Fragkoudi, F., Querejeta, M., et al. 2019, MNRAS, 488, 3904
Lee, M. G., & Jang, I. S. 2016, ApJ, 819, 77
Lemonias, J. J., Schiminovich, D., Thilker, D., et al. 2011, ApJ, 733, 74
Leroy, A. K., Walter, F., Brinks, E., et al. 2008, AJ, 136, 2782
Lian, J., Yan, R., Blanton, M., & Kong, X. 2017, MNRAS, 472, 4679
MacArthur, L. A., Courteau, S., Bell, E., & Holtzman, J. A. 2004, ApJS,
   152, 175
Martin, D. C., Fanson, J., Schiminovich, D., et al. 2005, ApJL, 619, L1
Mo, H. J., Mao, S., & White, S. D. M. 1998, MNRAS, 295, 319
Morrissey, P., Conrow, T., Barlow, T. A., et al. 2007, ApJS, 173, 682
Mullan, B., Kepley, A. A., Maybhate, A., et al. 2013, ApJ, 768, 194
Muñoz-Mateos, J. C., Boissier, S., Gil de Paz, A., et al. 2011, ApJ, 731, 10
Muñoz-Mateos, J. C., Gil de Paz, A., Boissier, S., et al. 2007, ApJ, 658, 1006
Muzzin, A., Wilson, G., Yee, H. K. C., et al. 2012, ApJ, 746, 188
Naab, T., & Ostriker, J. P. 2006, MNRAS, 366, 899
Padave, M., Borthakur, S., Gim, H. B., et al. 2021, ApJ, 923, 199
Pejcha, O., & Prieto, J. L. 2015, ApJ, 799, 215
Peng, Y., Maiolino, R., & Cochrane, R. 2015, Natur, 521, 192
```

Samland, M., & Gerhard, O. E. 2003, A&A, 399, 961

```
Peng, Y.-j., Lilly, S. J., Kovač, K., et al. 2010, ApJ, 721, 193
Pezzulli, G. 2021, MNRAS, 508, 5842
Pezzulli, G., Fraternali, F., Boissier, S., & Muñoz-Mateos, J. C. 2015,
   MNRAS, 451, 2324
Pilkington, K., Few, C. G., Gibson, B. K., et al. 2012, A&A, 540, A56
Rafelski, M., Gardner, J. P., Fumagalli, M., et al. 2016, ApJ, 825, 87
Rafelski, M., Rose, S., Toolan, S., et al. 2018, COS Data Handbook v4.0
   (Baltimore, MD: STScI)
Renzini, A., & Peng, Y.-j 2015, ApJL, 801, L29
Rieke, G. H., Young, E. T., Engelbracht, C. W., et al. 2004, ApJS, 154, 25
Rodríguez-Puebla, A., Primack, J. R., Avila-Reese, V., & Faber, S. M. 2017,
   MNRAS, 470, 651
Roškar, R., Debattista, V. P., Brooks, A. M., et al. 2010, MNRAS, 408,
Roškar, R., Debattista, V. P., Stinson, G. S., et al. 2008, ApJL, 675, L65
Sabbi, E., Calzetti, D., Ubeda, L., et al. 2018, ApJS, 235, 23
Sacchi, E., Cignoni, M., Aloisi, A., et al. 2019, ApJ, 878, 1
Saintonge, A., & Catinella, B. 2022, ARA&A, 60, 319
Salim, S., Rich, R. M., Charlot, S., et al. 2007, ApJS, 173, 267
Salpeter, E. E. 1955, ApJ, 121, 161
```

```
546, A2
Sancisi, R., Fraternali, F., Oosterloo, T., & van der Hulst, T. 2008, A&ARV,
  15, 189
Schlafly, E. F., & Finkbeiner, D. P. 2011, ApJ, 737, 103
Smith, M. V., van Zee, L., Dale, D. A., et al. 2022, MNRAS, 515, 3270
Somerville, R. S., Barden, M., Rix, H.-W., et al. 2008, ApJ, 672, 776
Sommer-Larsen, J., & Dolgov, A. 2001, ApJ, 551, 608
Sorce, J. G., Tully, R. B., Courtois, H. M., et al. 2014, MNRAS, 444, 527
Steinhauser, D., Schindler, S., & Springel, V. 2016, A&A, 591, A51
Thilker, D. A., Bianchi, L., Meurer, G., et al. 2007, ApJS, 173, 538
Tully, R. B., Courtois, H. M., & Sorce, J. G. 2016, AJ, 152, 50
van Dokkum, P. G. 2001, PASP, 113, 1420
van Dokkum, P. G., Leja, J., Nelson, E. J., et al. 2013, ApJL, 771, L35
Wang, J., Kauffmann, G., Overzier, R., et al. 2011, MNRAS, 412, 1081
White, S. D. M., & Frenk, C. S. 1991, ApJ, 379, 52
Williams, B. F., Dalcanton, J. J., Dolphin, A. E., Holtzman, J., & Sarajedini, A.
  2009, ApJL, 695, L15
Wright, E. L., Eisenhardt, P. R. M., Mainzer, A. K., et al. 2010, AJ, 140, 1868
Yang, X., Mo, H. J., van den Bosch, F. C., et al. 2007, ApJ, 671, 153
Yoon, J. H., & Putman, M. E. 2013, ApJL, 772, L29
```

Sánchez, S. F., Rosales-Ortega, F. F., Marino, R. A., et al. 2012, A&A,